JOURNAL OF PETROLOGY

Journal of Petrology, 2020, Vol. 61, No. 8: egaa084
doi: 10.1093/petrology/egaa084
Advance Access Publication Date: 26 August 2020
Original Article

OXFORD

Petrology of the April 2015 Eruption of Calbuco Volcano, Southern Chile

Olivier Namur[1,2]*, Salvatrice Montalbano[2], Olivier Bolle[2] and Jacqueline Vander Auwera[2]

[1]Department of Earth and Environmental Sciences, KU Leuven, Heverlee 3001, Belgium; [2]Department of Geology, University of Liège, Liège 4000, Belgium

*Corresponding author. Telephone: +32 16 37 65 38; Fax: +32 16 32 29 80; E-mail: olivier.namur@kuleuven.be

Received 7 August 2019; Accepted 18 August 2020

ABSTRACT

Understanding the origin of intermediate magmas that commonly erupt from subduction zone volcanoes is important to better constraining the mechanisms of continental crust formation. We performed a detailed mineralogical and petrological study of the eruptive products from the April 2015 eruption of Calbuco volcano, Chile, a three-phase sub-Plinian eruption that produced pyroclastic deposits of andesitic composition. The eruptive products comprise a glass phase and a high but variable proportion of minerals dominated by plagioclase, clinopyroxene, and orthopyroxene, with minor olivine, amphibole, and magnetite. Plagioclase is very strongly zoned with highly anorthitic cores surrounded by more albitic rims, and no intermediate compositions between them. Based on thermodynamic calculations and published experimental data, we estimate that the anorthitic cores crystallized from a basaltic andesite melt containing 3·5–4·5 wt% H_2O. The bulk-rock major and trace element variability at Calbuco is best explained by the accumulation of a variable amount of minerals (in relative proportion 72 % plagioclase, 28 % pyroxene) in a dacitic melt. These minerals most probably formed in the crystal mush zone of the magma chamber, at 200–300 MPa (8–11 km depth) according to pyroxene and amphibole compositions. A few weeks to months before the eruption, the crystal mush was disaggregated, perhaps owing to magmatic underplating, and a crystal-bearing dacitic melt migrated into a subsurface storage region where the albitic plagioclase rims crystallized. The eruption was probably internally triggered by over-pressurization in the shallow magma chamber.

Key words: Andes; subduction; plagioclase; plumbing system; water

INTRODUCTION

The origin of andesitic magmas remains debated, and models for their formation include the melting of hydrous mantle domains, fractional crystallization of basaltic magmas, and/or magma mixing (Grove & Kinzler, 1986). Correspondingly, the deep structure of andesitic volcanoes, which dominantly occur in subduction zones, is also debated, with some models suggesting magma storage and differentiation at the Moho (e.g. Annen *et al.*, 2006, 2015) whereas many others provide strong evidence for differentiation at upper crustal pressures (e.g. Almeev *et al.*, 2013; Ruth *et al.*, 2016; Stechern *et al.*, 2017; Vander Auwera *et al.*, 2019). Understanding the origin of andesites is crucial because the continental crust, broadly andesitic to dacitic in composition, has been primarily built at subduction zones since at least the Proterozoic (Taylor & McLennan, 1985; Rudnick & Gao, 2003). Furthermore, the volatile-rich nature of andesitic calc-alkaline magmas leads to explosive and locally devastating eruptions, often with very little warning (Stock *et al.*, 2016).

Andesitic lavas are rich in crystals that often show various textures such as compositional zoning or resorption (Anderson, 1976; Eichelberger, 1978;

Nakamura, 1995; Browne *et al.*, 2006; Eichelberger *et al.*, 2006; Humphreys *et al.*, 2006, 2009; Streck, 2008; Kent *et al.*, 2010; Cashman & Blundy, 2013; Higgins *et al.*, 2015; Kahl *et al.*, 2015; Ruth *et al.*, 2016). It is now recognized that volcanic rocks represent the eruptive products of the mobile part of crystal mushes (Bachmann & Bergantz, 2004; Bachmann *et al.*, 2007; Kent *et al.*, 2010; Burgisser & Bergantz, 2011; Cooper & Kent, 2014; Annen *et al.*, 2015). Consequently, the crystals observed in andesitic lavas partly represent disaggregated crystal mushes (Bachmann & Bergantz, 2003; Huber *et al.*, 2010, 2011; Burgisser & Bergantz, 2011; Ellis *et al.*, 2014) and may therefore record deep differentiation processes (e.g. Izbekov *et al.*, 2002; Streck, 2008; Cashman & Blundy, 2013; Cashman *et al.*, 2017) and their timescales (e.g. Cooper & Reid, 2003; Cooper & Kent, 2014; Conway *et al.*, 2020). The full integration of geochemical data on andesitic magmas (e.g. Baker *et al.*, 1994; Grove *et al.*, 2002; Ruprecht *et al.*, 2012; Wanke *et al.*, 2019), detailed analyses of their crystal cargoes (e.g. Browne *et al.*, 2006; Streck, 2008; Kent *et al.*, 2010; Higgins *et al.*, 2015), and results of phase equilibria studies (Sisson & Grove, 1993; Scaillet & Evans, 1999; Grove *et al.*, 2003; Holtz *et al.*, 2004; Botcharnikov *et al.*, 2008; Parat *et al.*, 2014; Melekhova *et al.*, 2015) is therefore critical to improving our understanding of subduction zone volcanoes.

In this study, we integrate bulk-rock chemistry with mineral chemistry and textural analyses of a large sample suite from the April 2015 eruption of Calbuco volcano, Chile, and combine our data with previous smaller sample sets (Arzilli *et al.*, 2019; Morgado *et al.*, 2019*a*). We propose that a significant portion of the crystal cargo originated from disaggregated crystal mushes (Morgado *et al.*, 2019*a*) and was transported through several storage regions before eruption. We estimate the effects of crystal accumulation on bulk-rock chemistry and suggest that crystal accumulation is an important mechanism during the formation of intermediate magmas. We compare our results with a compilation of high-temperature experiments on intermediate magmas and discuss crystal formation conditions at Calbuco. In particular, we suggest that plagioclase and mafic crystals predominantly crystallized from a hydrous melt at ~11 km depth and were subsequently transported to a shallow storage region a few weeks to months before the 2015 eruption.

CALBUCO VOLCANO AND THE 22–23 APRIL 2015 ERUPTION

Calbuco (41°20′S, 72°37′W, summit elevation 2003 m above sea level) is one of around 20 historically active volcanoes in the Southern Volcanic Zone (SVZ) of the Andes. The SVZ (33–46°S) results from the subduction of the Nazca plate under the South American plate (Stern, 2004) and is subdivided into the northern (NSVZ, 33°–34°30′S), transitional (TSVZ, 34°30′–37°S), central (CSVZ, 37°–41°30′S), and southern regions (SSVZ, 41°30′–46°S). The compositions of lavas erupted along the SVZ continuously change from andesite and dacite in the NSVZ to basaltic andesite and basalt in the SSVZ. Crustal thickness in the SVZ decreases from 55–60 km in the NSVZ to 35–55 km in the TSVZ and <30–35 km in the CSVZ and SSVZ (Assumpção *et al.*, 2013; Hickey-Vargas *et al.*, 2016). Beneath Calbuco, the crustal thickness is ~30 km (Syracuse *et al.*, 2010).

Calbuco is a composite volcano with a truncated cone that covers an area of 150 km^2. It was built over the last ~300 kyr, and more than 40 major pyroclastic density current (PDC) and pumice fall deposits are intercalated with postglacial sedimentary rocks (<13 ka; Moreno & Naranjo, 2004; Watt *et al.*, 2011). Calbuco predominantly produces lava flows (basaltic andesite to andesite) and explosive eruptions producing tephra falls, PDCs, block-and-ash flows, and lahars, although andesitic to dacitic domes have also been extruded (Lopez-Escobar *et al.*, 1992, 1995; Castruccio *et al.*, 2010; Castruccio & Clavero, 2015). Eruptive products at Calbuco are generally more evolved than those of the nearby (within ~20 km) Osorno and La Picada volcanoes, which mostly erupt basalts and basaltic andesites (Lopez-Escobar *et al.*, 1992, 1995; Vander Auwera *et al.*, 2019).

The evolution of Calbuco is divided into four stages (Sellés & Moreno, 2011; Romero *et al.*, 2016): Calbuco 1 (340–110 ka) dominantly consists of basaltic andesite; Calcubo 2 (110–14 ka) is represented by glacially eroded andesites and dacites; Calbuco 3 (<14 ka to Holocene) is dominated by basaltic andesites and dacites, and two major sector collapses of the main edifice occurred during this period; and Calbuco 4 (historical eruptions) produced basaltic andesite to andesitic lava flows, block-and-ash flows, tephra falls, lahars, and a lava dome. Twelve historical eruptions have been described since 1792, including the 22–23 April 2015 eruption. The highest intensity historical eruption at Calbuco occurred in 1893.

The 2015 eruption of Calbuco started on 22 April (18:05 local time) following a 3 month period of increased local low-magnitude volcano-tectonic (VT) seismicity. During the prior few years and before January 2015, no more than five seismic events were recorded per month. From 1 January to 21 April 2015, 147 seismic events, including 142 VT events, were recorded, and a swarm of 140 VT events occurred 3 h before the start of the eruption. No significant deformation of the edifice was observed prior to the eruption, although 12 cm of subsidence with a source depth of 8–11 km beneath the edifice was identified from a Sentinel-1 interferogram acquired during the eruption (Delgado *et al.*, 2017). The first eruptive phase occurred in the summit crater and produced a 15 km high eruptive column that lasted 1·5 h. The second eruptive phase started on 23 April (01:00 local time) and produced a 17 km high plume that lasted 6 h, followed by a third waning phase of sporadic, minor eruptive events through 30 April. The two major eruptive phases

emplaced at least nine successive PDCs (A–I; Castruccio *et al.*, 2016), the largest of which travelled 6 km from the vent on the NE and SW flanks. Lahars travelled 10 km from vent on the south flank. Tephra falls occurred mainly to the NE, forming four main layers of 50 cm total thickness 6 km from vent and 5 cm total thickness 27 km from vent (Castruccio *et al.*, 2016; Romero *et al.*, 2016). PDC deposits emplaced during this eruption cover an area of 650 000 m^2. The total volume of eruptive products, as reconstructed from field measurements of tephra thicknesses or radar interferometric observations, is ~0·27–0·60 km^3 (Castruccio *et al.*, 2016; Romero *et al.*, 2016; Van Eaton *et al.*, 2016; Delgado *et al.*, 2017). Deposits are dominated by brown to grey vesicular (15–20 vol%) to highly vesicular (40–60 vol%) basaltic andesite scoria containing 25 vol% crystals (plagioclase, clinopyroxene, and orthopyroxene, with minor Fe–Ti oxides, amphibole, and olivine; Castruccio *et al.*, 2016; Arzilli *et al.*, 2019). This eruption was triggered by either over-pressurization owing to second boiling in the mush (Arzilli *et al.*, 2019) or a magma replenishment event (Morgado *et al.*, 2019*a*, 2019*b*).

SAMPLING AND ANALYTICAL METHODS

Sampling

Twenty-seven samples were collected in April–May 2015 and January 2016, eight of which (labeled 'KAL' and collected in 2015) were briefly described by Castruccio *et al.* (2016) but were re-analyzed in this study. Castruccio *et al.* (2016) attributed these samples to tephra fall layers 1 and 3 and to PDC units B, C, and I. Samples from PDCs are centimeter- to decimeter-scale pumiceous bombs. All samples collected in January 2016 are from tephra fall deposits, but it was not possible to attribute them to specific fall layers. Four of these samples are from centimeter- to decimeter-scale pumiceous bombs or blocks. Other samples mostly comprise grey to brown or black pyroclasts and scoria lapilli with millimeter- to centimeter-scale glassy, vesicular, and subangular lithic fragments that can be attributed to the brown scoria and dark grey, dense juvenile fragments described by Castruccio *et al.* (2016). Sample locations are shown in Fig. 1 and reported in Supplementary Dataset 1; supplementary data are available for downloading at http://www.petrology.oxfordjournals.org.

Methods

Petrographic methods

We refer to crystals with a long dimension of at least 150 μm as macrocrysts and smaller crystals as microcrysts. We favor the term 'macrocryst' (e.g. Ruprecht *et al.*, 2012) because 'phenocryst' often carries a genetic connotation, and it is now recognized that crystals in lavas are often in disequilibrium with their carrier liquids (e.g. Ganne *et al.*, 2018).

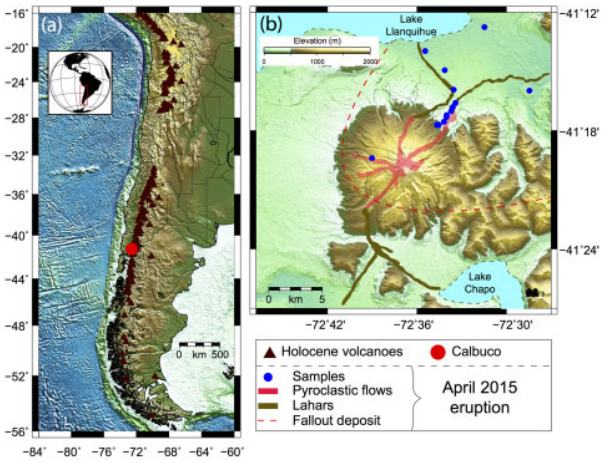

Fig. 1. Location of Calbuco volcano and sampling points. (a) Topographic map (SRTM 2.1 digital elevation model) of the Andean Southern Volcanic Zone (SVZ) showing the position of Calbuco and other Holocene volcanoes. (b) Topographic map (ETOPO1 global relief model) of Calbuco, pyroclastic fall and density current deposits and lahars resulting from the April 2015 eruption (Castruccio *et al.*, 2016), and our sampling locations.

Sample petrography was observed using a Nikon optical microscope under transmitted and reflected light. For most samples, back-scattered electron (BSE) images were also acquired with a QEMSCAN FEI Quanta 650F (Rheinisch-Westfälische Technische Hochschule, Aachen University) or a JEOL JSM-7610F (Institute of Mineralogy, Leibniz University, Hannover) using an acceleration voltage of 10 kV, a beam current of ~1 nA, a fixed working distance of 9 mm, and a 60 nm aperture; electron micrographs were captured with a dwell time of 10 μs. Energy-dispersive X-ray (EDX) mapping of plagioclase crystals was performed using two Bruker Quantax XFlash 6-60 EDX detectors fitted on the JSM-7610F. The macrocryst phase proportions and vesicularities of 13 samples were determined by point counting, and plagioclase macrocryst crystal size distributions (CSDs) were calculated for five selected samples (details are given in Appendix A).

X-ray fluorescence

Bulk-rock major and selected trace element (Co, Cu, Ni, Rb, Sr, Y, Zn, Zr, Ba, Cr, V) concentrations were measured by X-ray fluorescence (XRF) with an ARL PERFORM-X 4200 (Rh X-ray tube) at the University of Liège (Belgium) following the procedure of Vander Auwera *et al.* (2019; see Appendix A).

Inductively coupled plasma mass spectrometry

For most samples, trace element analyses were also performed by inductively coupled plasma mass spectrometry (ICP-MS) using a ThermoFisher Scientific X-Series 2 at the Royal Museum for Central Africa [Tervuren, Belgium; see details given by Vander Auwera *et al.* (2019)]. We measured ^{45}Sc, ^{51}V, ^{53}Cr,

^{59}Co, ^{60}Ni, ^{63}Cu, ^{66}Zn, ^{68}Ga, ^{70}Ge, ^{85}Rb, ^{88}Sr, ^{89}Y, ^{91}Zr, ^{93}Nb, ^{133}Cs, ^{137}Ba, ^{139}La, ^{140}Ce, ^{141}Pr, ^{143}Nd, ^{147}Sm, ^{153}Eu, ^{157}Gd, ^{159}Tb, ^{163}Dy, ^{165}Ho, ^{167}Er, ^{169}Tm, ^{173}Yb, ^{175}Lu, ^{180}Hf, ^{181}Ta, ^{184}W, ^{208}Pb, ^{232}Th, and ^{238}U. Details on the procedure, accuracy, and precision are given in Appendix A.

Electron probe microanalysis

The major element compositions of minerals and naturally quenched glasses were measured with a Cameca SX100 electron probe microanalyser (EPMA) at the Institute of Mineralogy, Leibniz University, Hannover. Glasses were measured using a defocused beam (spot size 2 or 5 μm), a 15 kV accelerating voltage, and an 8 nA beam current. To minimize alkali loss, Na and K were measured first on two different spectrometers. Mineral analyses were performed using a focused beam (1 μm spot size) with a current of 15 nA. Counting times were 15–20 s on-peak (7·5–10 s background) for each element. We used a calibration identical to that of Namur & Charlier (2017). Details on the calibration, accuracy, and precision are given in Appendix A.

Laser ablation inductively coupled plasma mass spectrometry

In situ mineral (cores and rims of plagioclase, clinopyroxene, orthopyroxene, and amphibole) and glass trace element analyses were performed by laser ablation ICP-MS (LA-ICP-MS) at the Institute of Mineralogy, Leibniz University, Hannover, with a ThermoScientific ElementXR ICP-MS system coupled with a Spectra Physics Solstice 194 nm femtosecond laser. The following isotopes were measured in low-mass-resolution mode: ^{23}Na, ^{25}Mg, ^{27}Al, ^{29}Si, ^{31}P, ^{39}K, ^{43}Ca, ^{45}Sc, ^{47}Ti, ^{49}Ti, ^{51}V, ^{53}Cr, ^{55}Mn, ^{57}Fe, ^{60}Ni, ^{85}Rb, ^{88}Sr, ^{89}Y, ^{91}Zr, ^{137}Ba, ^{139}La, ^{140}Ce, ^{141}Pr, ^{143}Nd, ^{147}Sm, ^{153}Eu, ^{157}Gd, ^{159}Tb, ^{163}Dy, ^{165}Ho, ^{167}Er, ^{169}Tm, ^{173}Yb and ^{175}Lu. The procedure and calibration have been described by Neave *et al.* (2018) and are given in Appendix A.

Homogenization and analysis of melt inclusions

Olivine, a minor phase at Calbuco, contains well-shaped, rounded, melt inclusions. Although rare inclusions were naturally quenched, others present daughter phases. Crystal-bearing olivine-hosted inclusions ($n = 48$) from three samples were re-homogenized by heating to their melting point (i.e. until all daughter minerals disappeared). Only melt inclusions far from crack planes and the host crystal rim were selected. Homogenization experiments (Supplementary Data Fig. 1) were performed at the Laboratoire Magmas et Volcans (Clermont-Ferrand, France) using a heating–quenching stage attached to a petrographic microscope (Schiavi *et al.*, 2016). Details on the heating procedure and correction for post-entrapment crystallization are given in Appendix A. The compositions of re-homogenized inclusions were subsequently measured by EPMA.

Naturally quenched pyroxene-hosted melt inclusions were observed in some samples. We measured their compositions in one of our tephra samples by EPMA. Compositions were not corrected for post-entrapment crystallization (Neave *et al.*, 2017*b*).

RESULTS

Petrography

Samples are variably vesicular (from <10 to >50 vol% vesicles) and contain crystals of various sizes (Fig. 2a). Macrocrysts are dominated by plagioclase, clinopyroxene, and orthopyroxene (Figs 2 and 3), with minor magnetite, olivine, and amphibole. In many samples, we observed aggregated macrocrysts forming glomerocrysts (Fig. 4). Isolated macrocrysts and glomerocrysts are embedded in quenched glass (Fig. 2b) or less commonly in a fine-grained matrix (<10–150 μm; Fig. 2c–d) strongly dominated by unzoned or slightly zoned tabular plagioclase and minor pyroxene and magnetite. In glassy samples, the glass phase locally contains very small (usually <10 μm, but up to 50 μm) quench crystals dominated by unzoned skeletal plagioclase. Microcrysts therefore show a bimodal size distribution comprising the fine-grained matrix and quench crystals in glassy areas [termed 'blocky microlites' and 'skeletal microlites', respectively, by Arzilli *et al.* (2019)]. According to Arzilli *et al.* (2019), the glass/microlite ratio is ~2·5/1.

Mafic minerals are strongly dominated by subhedral to euhedral, blocky to elongate clinopyroxene and orthopyroxene (Fig. 2b–f) that are generally unzoned, although minor zoning was observed in rare samples (Fig. 2d). They often contain glassy melt inclusions and crystal inclusions, generally Fe–Ti oxides. In all samples, pyroxene macrocrysts are relatively small and rarely exceed 200–300 μm in length [up to 700 μm according to Arzilli *et al.* (2019)]. Rounded to subhedral magnetite crystals 20–50 μm in size are commonly observed; according to our nomenclature (see 'Methods'), we consider them to be microcrysts, although they are much larger than quench crystals in the glass phase (Fig. 2b) and most crystals forming the fine-grained matrix (Fig. 2d). This may indicate that our arbitrary threshold between microcryst and macrocryst was too large. It should also be noted that Arzilli *et al.* (2019) described rounded magnetite crystals up to 300 μm in diameter. Olivine is present in most samples as a minor phase, often in glomerocrysts, and always occurs as moderately small (100–300 μm) anhedral crystals partly dissolved and replaced by orthopyroxene, locally forming a symplectitic texture with magnetite (Fig. 2e). The junction between individual symplectitic orthopyroxene crystals is usually filled with glass, indicating that olivine reacted with the melt to form orthopyroxene ± magnetite. Amphibole was only observed in a single sample, and forms 200–500 μm long subhedral to euhedral, blocky to elongate, brown to green crystals, some containing a core of anhedral, resorbed orthopyroxene. Larger, poikilitic amphibole crystals (up to 1 mm) also

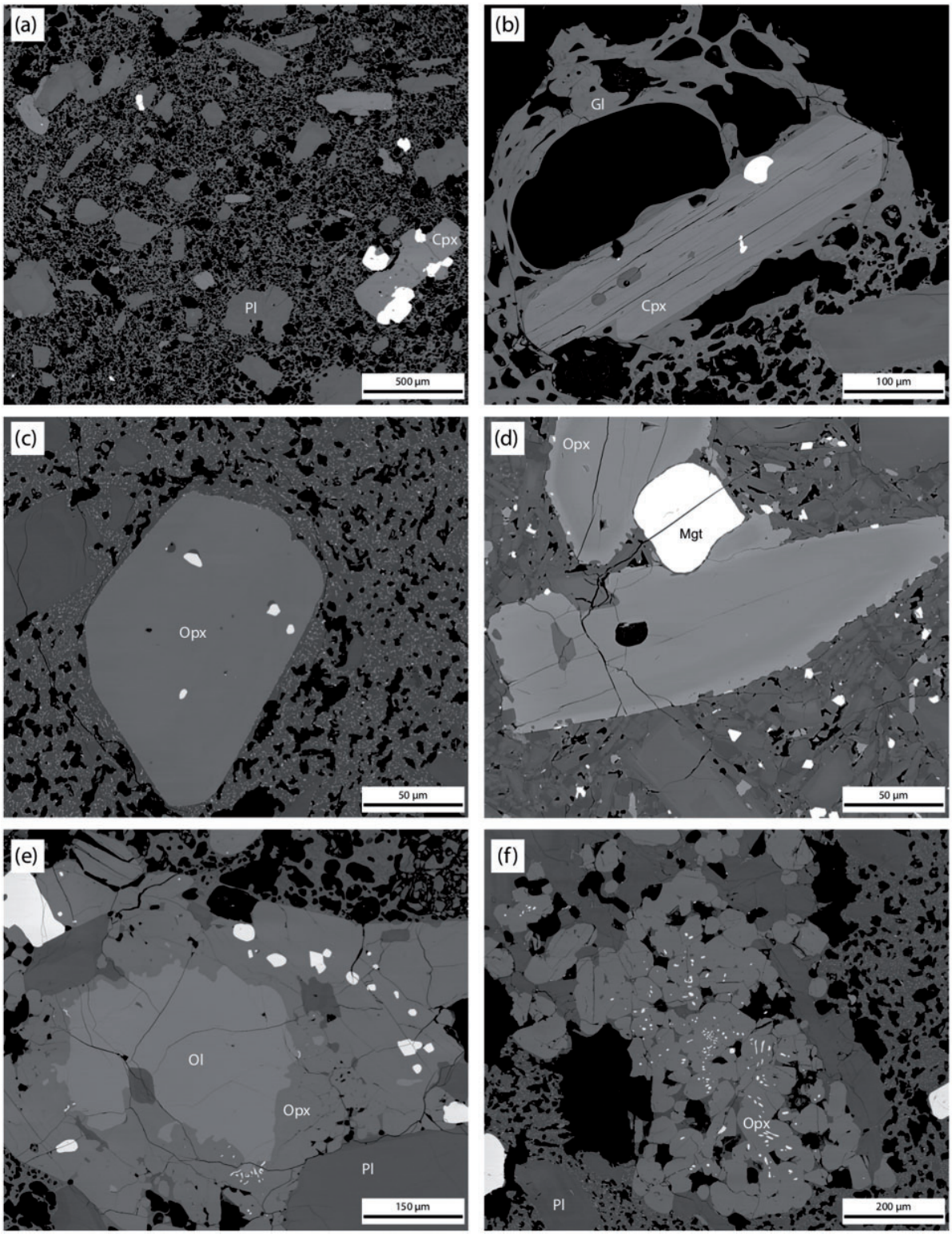

Fig. 2. Mineralogy and textures of samples from the 2015 Calbuco eruption. (a) Overview of a representative sample (CL141) showing a glassy vesicle-rich matrix and small (<20 μm) to large (>50 μm) crystals dominated by plagioclase, pyroxene (clinopyroxene and orthopyroxene), and magnetite (bright phase). (b) Enlarged view of a euhedral clinopyroxene. Noteworthy features are the presence of melt and magnetite inclusions within the crystal, and the surrounding glassy matrix. (c) Large subhedral orthopyroxene crystal. It should be noted that the matrix around the crystal comprises a mixture of glass and tiny (~1 μm) groundmass crystals of plagioclase, pyroxene, and Fe–Ti oxides. (d) Slightly zoned orthopyroxene crystals. (e) Crystal aggregate (glomerocryst) dominated by mafic phases. It should be noted that olivine is strongly anhedral and has partly been replaced by orthopyroxene. (f) Glomerocryst dominated by orthopyroxene and plagioclase crystals.

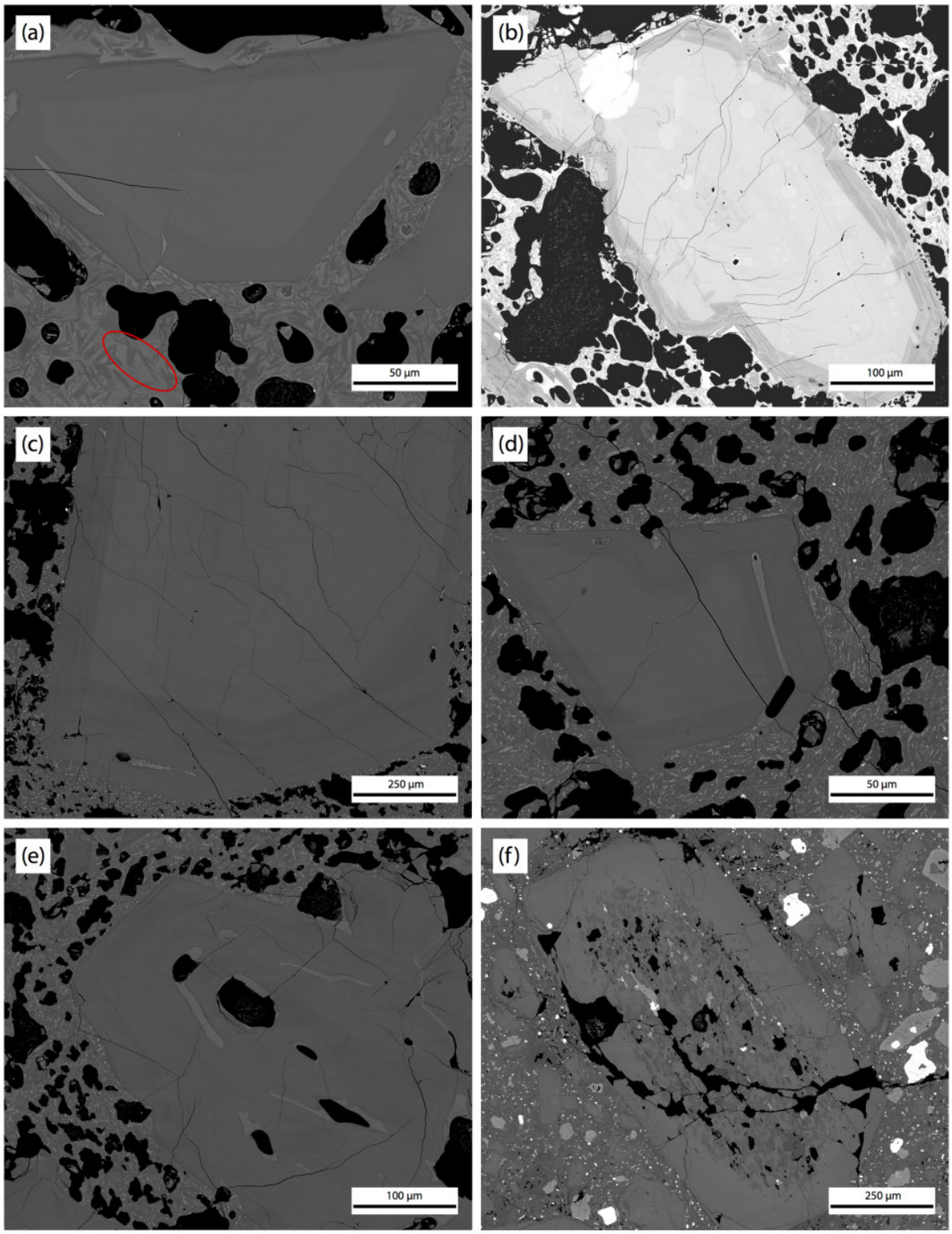

Fig. 3. Textural features of plagioclase crystals. Back-scattered electron images illustrating various textures of plagioclase crystals. (a–c) Strongly zoned tabular phenocrysts with relatively homogeneous, An-rich cores surrounded by more albitic oscillatory-zoned rims. The skeletal crystals [red oval in (a)] in the fine-grained, partially glassy matrix should be noted. (d, e) Examples of plagioclase phenocrysts showing melt resorption channels at the core–rim interface or within the crystal core. (f) Example of a very rare group of crystals showing a normally zoned, euhedral, ~200 μm wide overgrowth on a resorbed, sieve-textured core.

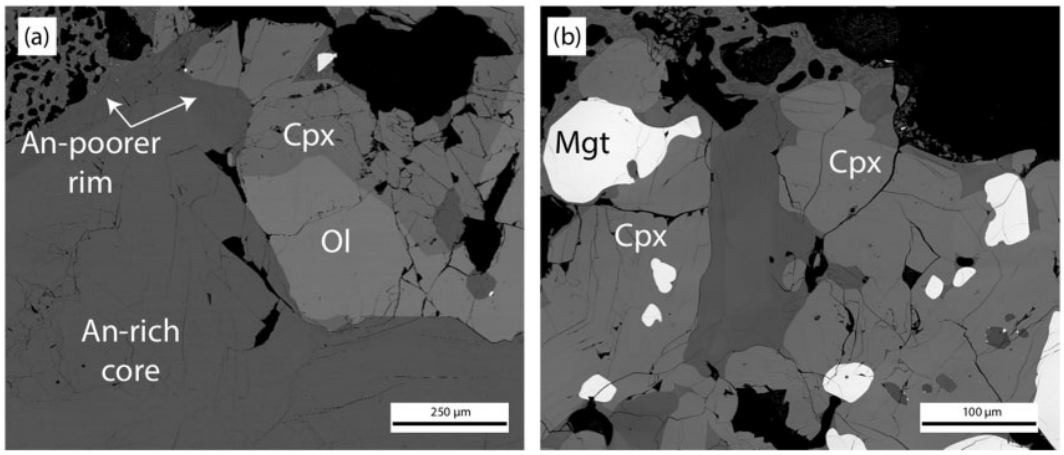

Fig. 4. Textural features of plagioclase crystals in glomerocrysts. (a) Close-up view of the edge of a large plagioclase crystal in a glomerocryst. The presence of the An-poor rim at the contact with the glassy matrix, but the absence of plagioclase zoning at the interface between plagioclase and clinopyroxene or orthopyroxene, should be noted. (b) Plagioclase crystal in a plagioclase–pyroxene–magnetite glomerocryst. It should be noted that the plagioclase core is surrounded by a thick, relatively An-poor rim.

occur, and generally enclose small, zoned plagioclase crystals.

Plagioclase (Fig. 3) is by far the major crystal phase, with a matrix- and pore-free modal proportion of 61–90 wt% (Supplementary Data Fig. 2). Plagioclase crystals vary in size from microcrysts (<150 μm) in the glass phase and fine-grained matrix to small (100–300 μm) and very large (up to 8 mm) macrocrysts. Microcrysts show prismatic elongation with euhedral morphology or acicular elongation with hopper, swallowtail, or skeletal morphology (Fig. 3a; see also fig. 2a of Arzilli *et al.*, 2019). Skeletal crystals most probably formed by quenching during strong undercooling (Shea & Hammer, 2013). The great majority of plagioclase macrocrysts show a blocky or prismatic euhedral habit (Fig. 3b), although some rare crystals are partly to almost entirely resorbed.

We observed several plagioclase zoning textures, as follows.

(1) *Normal, stepped zonings*. Most plagioclase macrocrysts show a very strong normal zoning, with a sharp boundary between the crystal core and rim (Fig. 3a and b; Arzilli *et al.*, 2019; Morgado *et al.*, 2019*a*). Although variable and possibly correlated to crystal size, rim widths generally range from 30 to 80 μm, but exceed 250 μm in some crystals. The cores of such crystals are sometimes textureless, but more commonly show optical evidence of thin (2–10 μm) alternating darker and lighter zones defining oscillatory zoning. Rims show oscillatory zoning and appear significantly darker than the cores in BSE images (Fig. 3c).

(2) *Simple resorption zones and isolated inclusions*. In most plagioclase macrocrysts, the rims define concordant, euhedral growth over a euhedral core. However, in some crystals, dissolution features such as resorption interfaces, as observed by Morgado *et al.* (2019*a*), may attest to changes in magma composition or crystal equilibration pressure (Bennett *et al.*, 2019). In most cases, dissolution features are embayed core–rim boundaries or dissolution channels within the crystal (Fig. 3d and e). Although Arzilli *et al.* (2019) described naturally quenched, isolated, plagioclase-hosted melt inclusions in rocks from the 2015 Calbuco eruption, we observed only a single inclusion with a well-rounded shape, and we suspect that some of the inclusions they described may be melt dissolution channels rather than actual melt inclusions.

(3) *Patchy zonings*. In some crystals, dissolution was highly pervasive and affected the entire crystal core, leading to cellular mineral structures with spongy appearances (Fig. 3f). In these crystals, cores usually show irregularly distributed zoning features, termed 'patchy zoning'. Such cores also commonly contain abundant melt droplets that represent either properly closed melt inclusions or sections of reactive melt channels (Nakamura & Shimakita, 1998). Solid inclusions and fluid bubbles are also commonly observed in patchy cores.

(4) *Unzoned crystals or crystal faces*. Isolated plagioclase macrocrysts are always zoned. In contrast, glomerocrystic plagioclase (Fig. 4a) usually do not show any zonings on crystal faces in contact with other crystals of the same glomerocryst. However, we noted some exceptions (Fig. 4b) in which the observed zoning could be due to a connection between plagioclase and melt in the third dimension, and thus not visible in thin section.

Plagioclase crystal size distributions (CSDs) have pronounced kinks at ~350–400 μm (square root of area, $A^{0.5}$; i.e. crystal length $L \approx 500$–700 μm) that separate shallow-gradient regressions on the population of large crystals from steep-gradient regressions on the population of small crystals (Fig. 5). As described in Appendix A, the accuracy of crystal-size measurements for small crystals ($A^{0.5} < 200$ μm) is questionable. Nevertheless, the two plagioclase populations hold when plagioclase population densities in $A^{0.5}$ bins <200 μm are removed

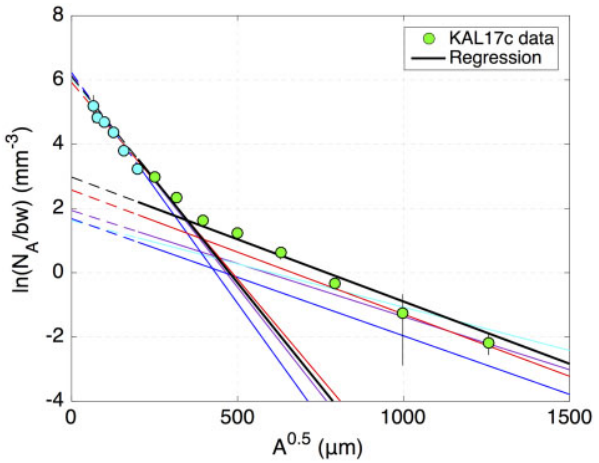

Fig. 5. Plagioclase size distribution. Plagioclase size distributions of representative samples, shown as crystal population density per unit area normalized by bin width (in mm^{-3}; $\ln(N_A/bw)$, where N_A is crystal number and bw is bin width) plotted against the square root of plagioclase area (in μm; $A^{0.5}$; Neave *et al.*, 2017*a*). Distributions were obtained from image analysis, and the data were processed using a geometric binning strategy (see Appendix A for details). No stereological conversion was applied. Distinct plagioclase populations are identified in all distributions. For sample KAL17c, data for the populations of small and large crystals are shown in blue and green, respectively. Thick black lines are linear regressions through each population in sample KAL17c with $r^2 > 0{\cdot}7$, and coloured lines are regressions for other samples (individual data not plotted).

from the linear regressions. Such kinked CSDs are best modeled as a mixture of two crystal populations, one of small crystal size and one of large crystal size (e.g. Marsh, 1998; Higgins & Roberge, 2007; Salisbury *et al.*, 2008; Kent *et al.*, 2010; Neave *et al.*, 2014, 2017*a*). Characteristic crystal lengths (L_D = −1/slope) are 70–90 μm ($A^{0.5}$) for the population of small crystals and 600–1360 μm for the population of large crystals. Our CSDs are similar, although not identical, to those presented by Arzilli *et al.* (2019); they observed two kinks, one at $L \approx 50$ μm and another at $L \approx 400$–500 μm. The latter kink is identical to or only slightly displaced towards lower size values compared with that shown in Fig. 5, whereas we did not observe the former because crystals smaller than 150 μm were excluded from our analysis.

Bulk-rock and glass compositions

Major elements

Bulk-rock major element compositions define a restricted range (Supplementary Dataset 2), with most rocks plotting as basaltic andesites on the total alkalis vs silica diagram (not shown). Only two samples are more evolved and plot as andesites: one (CL135) was sampled in a very fine-grained tephra layer, whereas the other (KAL-62G) shows peculiar petrographic features, such as an albitic matrix, indicating that it might be a xenolithic block transported by the magma during the 2015 eruption. Harker diagrams for important major elements are shown in Fig. 6, where they are compared with published bulk-rock data for the 2015 eruption (Arzilli *et al.*, 2019; Morgado *et al.*, 2019*a*, 2019*b*). Although samples display a restricted compositional range, especially when the two most evolved samples are ignored, some geochemical trends are observed: MgO, MnO, CaO, and FeO_t contents continuously decrease whereas Na_2O, K_2O, and P_2O_5 continuously increase with increasing SiO_2 content. No obvious trends are observed for Al_2O_3 and TiO_2 (not shown).

As mentioned above, the matrix of Calbuco samples is usually glassy, but locally contains abundant microlites. We analysed well-quenched areas of the glass matrix free of microlites. The glass matrix (Supplementary Dataset 2) is more evolved than the bulk-rocks in all samples. Most glass analyses returned andesitic to dacitic compositions (61–64 wt% SiO_2), but two samples showed more evolved, rhyolitic compositions (KAL17C, KAL21). These two rocks show a much more crystalline, fine-grained matrix comprising extremely abundant microlites, and do not contain large glassy areas as observed in other samples; glass was observed only as micrometer-scale pockets between crystals. Therefore, these rhyolitic compositions probably represent the products of late-stage, post-eruptive crystallization, and not the pre-eruptive composition of the melt in the magma chamber. Accordingly, the glass compositions of these two samples are excluded from further discussion and are not plotted in Fig. 6. Glass data from all other samples plot along the extension of the bulk-rock geochemical trends.

Naturally quenched pyroxene- (four) and plagioclase-hosted (one) and re-homogenized olivine-hosted melt inclusions display a larger compositional range than the bulk-rocks (Supplementary Dataset 3). Pyroxene- and plagioclase-hosted inclusions, including those presented by Arzilli *et al.* (2019), contain 58–63 wt% SiO_2, compositions similar to or slightly more primitive than the glassy matrix observed in our samples. Olivine-hosted inclusions are more primitive (47–58 wt% SiO_2). Although we did not measure melt inclusion volatile contents, our analyses returned relatively low totals (94·6–96·7 wt%), perhaps suggesting a significant amount of dissolved H_2O. All melt inclusion major element trends are subparallel to but markedly off the bulk-rock trends. It is not impossible that the melt compositions were changed during the heating experiments or that post-entrapment crystallization was not fully accounted for in our numerical model used to recalculate the melt composition. Indeed, depletion in FeO has been attributed to re-equilibration between melt inclusions and their host olivines owing to post-entrapment crystallization (Kent, 2008). Alternatively, the strongly corroded textures of the olivine crystals may suggest their crystallization from melts compositionally different from those erupted in 2015, and therefore that olivine is in strong chemical disequilibrium with the carrier melt.

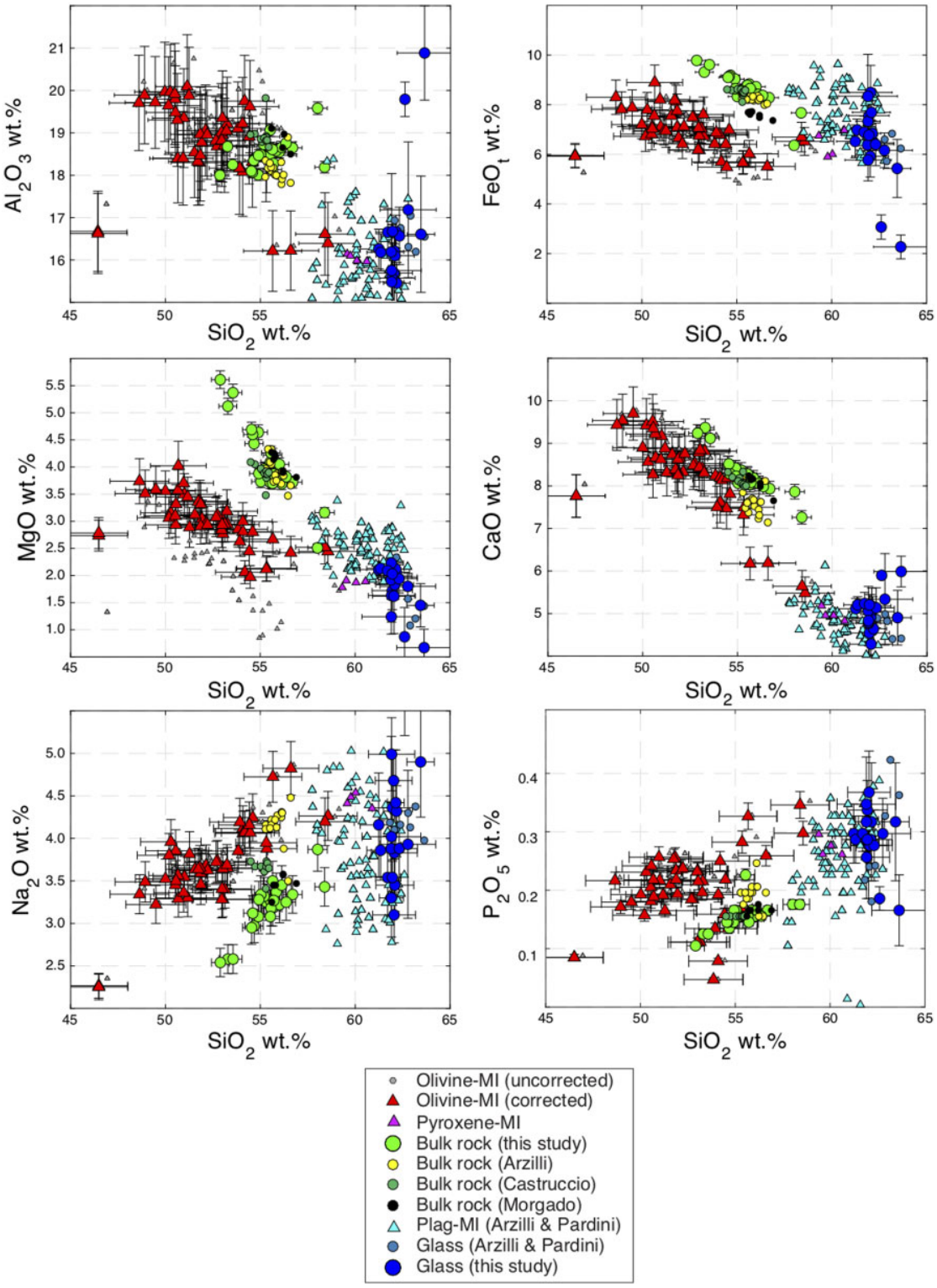

Fig. 6. Bulk-rock and glass major element compositions. Harker diagrams illustrating the behaviours of selected major elements, with SiO_2 chosen as the differentiation index. Red circles represent individual analyses of olivine-hosted melt inclusions in two samples corrected for post-entrapment crystallization. Error bars were estimated based on analytical errors and likely K_d^{Fe-Mg} values (Toplis, 2005). Error bars on XRF data or bulk-rock analyses from this study are based on repeated measurements and estimated analytical errors. Error bars are not shown for literature bulk-rock (XRF) data (Castruccio *et al.*, 2016; Arzilli *et al.*, 2019; Morgado *et al.*, 2019*b*). Glass data from this study are average values and 1σ errors based on ~20 analyses in each of 22 samples. Literature glass data are average values from four samples (Pardini *et al.*, 2018; Arzilli *et al.*, 2019). Literature plagioclase-hosted melt inclusion data are individual EPMA analyses in four samples (Pardini *et al.*, 2018; Arzilli *et al.*, 2019).

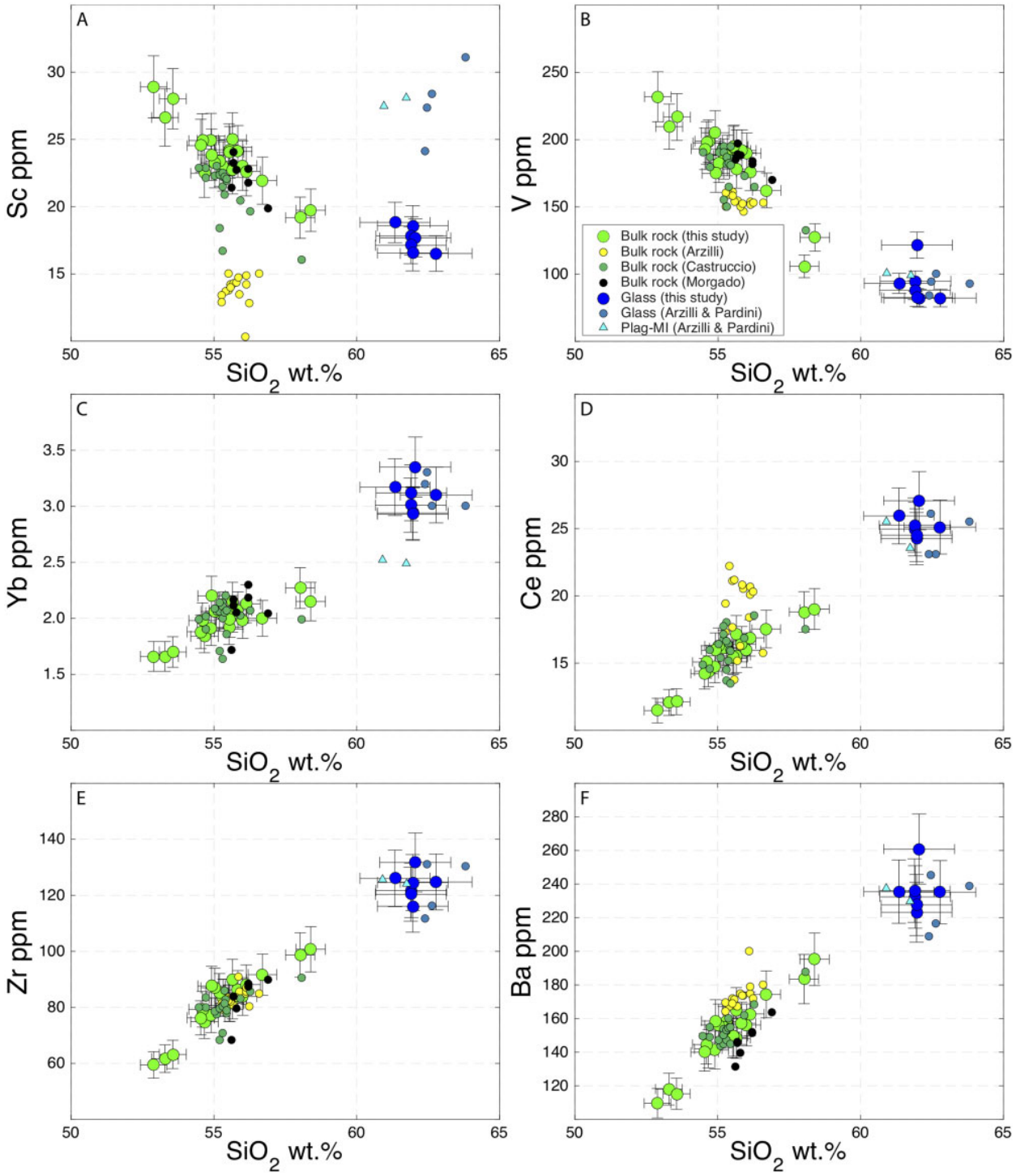

Fig. 7. Bulk-rock and glass trace element compositions. Harker diagrams illustrating the behaviours of selected trace elements, with SiO_2 chosen as the differentiation index. Error bars for XRF data or bulk-rock analyses from this study are based on repeated measurements and estimated analytical errors. Error bars are not shown for literature bulk-rock data (XRF and ICP-MS; Castruccio *et al.*, 2016; Arzilli *et al.*, 2019; Morgado *et al.*, 2019*b*). Glass data from this study are average values and 1σ errors based on ~20 analyses in each of 22 samples. Literature glass data are average values from four samples (Pardini *et al.*, 2018; Arzilli *et al.*, 2019). Literature plagioclase-hosted melt inclusion data are individual EPMA analyses in two samples (Pardini *et al.*, 2018; Arzilli *et al.*, 2019). Data from Morgado *et al.* (2019*b*) are not plotted for LREE because there are obvious errors in their data (i.e. Ce concentrations are lower than La concentrations).

Trace elements

When plotted against bulk-rock SiO_2 content, most bulk-rock trace element concentrations show clear geochemical trends (Fig. 7). For each trace element, we calculated the enrichment factor (E) between the samples with the highest and lowest SiO_2 contents. For convenience, we express this as log E such that all negative and positive values indicate depletion and enrichment, respectively. The concentrations of only a few trace elements (V, Co, Sc; log E = –0·26 to –0·17; Fig. 7a and b) continuously decrease with increasing SiO_2. In contrast, all others continuously increase with increasing SiO_2; the degree of enrichment is relatively modest for heavy rare earth elements (HREE; log E = 0·06–0·12; Fig. 7c), higher for light rare earth elements (LREE; log E = 0·13–0·22; Fig. 7d), and higher still for highly incompatible high field strength elements (HFSE; Zr, U, Th, Ta; log E = 0·23–0·33; Fig. 7e). Except Sr, large ion lithophile elements (LILE) also show strong enrichment (i.e. Cs, Ba, Rb; log E = 0·21–0·31; Fig. 7f). A few elements such as Sr, Cr, and Ni do not show any obvious trends with increasing SiO_2. In chondrite-normalized REE diagrams, all bulk-rock samples show parallel trends (Fig. 8a). We observed incoherent behaviours for La (not plotted in Fig. 8a) and Lu, which may be related to an analytical issue. Our samples are moderately enriched in REE (e.g. 19–31 and 10–14 times the Ce and Yb concentrations in CI chondrite, respectively). To evaluate the global behaviour of all REE, we used the model of O'Neill (2016) to calculate individual parameters that express the behaviour of all REE at once: λ_0 represents the average REE concentration normalized to CI chondrite, whereas λ_1 represents the slope of the CI-normalized REE pattern (reflecting LREE/HREE fractionation). These results show that REE concentrations increase with increasing bulk-rock SiO_2 content (Fig. 8b). The degree of LREE/HREE fractionation (calculated as Ce/Yb) also continuously increases from 1·92 to 2·46 with increasing SiO_2 content, as illustrated by the correlation between SiO_2 and λ_1 (Fig. 8c). When present, Eu anomalies [Eu/Eu*, where Eu* = $(Gd_N + Sm_N)/2$; the subscript 'N' denotes CI chondrite-normalized values] are small in magnitude (Eu/Eu* = 0·93–1·03).

Trace element concentrations in the glass matrix show a restricted compositional range and seem to plot along the extension of the bulk-rock trends (Fig. 7). To further evaluate this, we calculated the slopes of the trace element vs SiO_2 regressions including either the bulk-rocks alone or bulk-rocks + glass matrix. For all trace elements except Yb and Sc, the slope of the regressions changes by less than 20 % relative when including the glass matrix. In the REE diagram, glass matrix trends are parallel to the bulk-rock trends, but have higher REE concentrations (40–44 and 17–20 times Ce and Yb in CI chondrite, respectively). They show relatively constant degrees of LREE/HREE fractionation (Ce/Yb 2·22–2·33) and pronounced negative Eu anomalies (Eu/Eu* = 0·84–0·88).

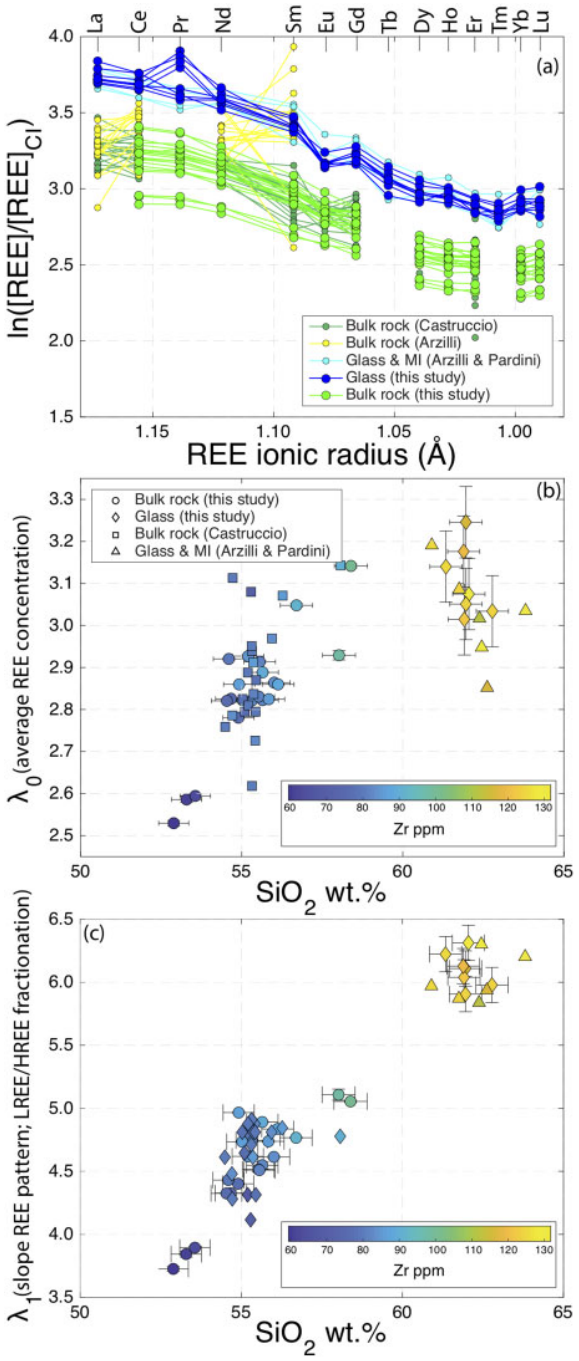

Fig. 8. Bulk-rock and glass rare earth element (REE) concentrations. (a) CI chondrite-normalized REE patterns (concentrations plotted against ionic radius; O'Neill, 2016). The trend of decreasing chondrite-normalized REE concentrations from LREE to HREE should be noted. (b) Evolution of λ_0 as a function of SiO_2 (chosen as the differentiation index). λ_0 was calculated using a polynomial fitting algorithm, and represents the average chondrite-normalized concentrations of individual samples (O'Neill, 2016). It should be noted that λ_0 also correlates with the concentrations of incompatible trace elements such as Zr. Error bars on the y-axis were obtained through Monte Carlo simulations in which we investigated how analytical errors affect λ_0; in many cases, the error bars are smaller than the symbol size. Error bars on the x-axis are as in Fig. 6. (b) Evolution of λ_1, representing the slope of the REE pattern (O'Neill, 2016), as a function of SiO_2.

Mineral compositions

Mafic minerals

We measured the major element compositions of clinopyroxene in 20 samples spanning the bulk-rock compositional range ($n = 1045$ individual measurements; Supplementary Dataset 4; average values are given in Supplementary Dataset 2). Clinopyroxene Mg# [molar $100 \times Mg/(Mg + Fe_t)$] ranges between 68·6 and 78·3 (mean = 73·8; $1\sigma = 1{\cdot}7$), similar to the previously reported range (66–75; Arzilli *et al.*, 2019; Morgado *et al.*, 2019*a*). Most data were collected along core–rim profiles. For each profile, we attempted to fit an error function and use the inflection in the derivative to automatically detect core, mantle, and rim compositional zones in the crystals (Namur *et al.*, 2014). We did not observe any inflections in clinopyroxene compositional profiles, indicating that clinopyroxene data are statistically and compositionally homogeneous at the crystal scale. To assess clinopyroxene compositional variability at the sample scale and eruption scale, we calculated Mg# probability density functions for each sample with more than 20 individual analyses and for our full dataset. The full clinopyroxene Mg# dataset can be adequately fitted by a single Gaussian distribution (Fig. 9a). We calculated the median of the clinopyroxene population to be 73·80 and the median absolute deviation (MAD) to be 1·00, a value identical to or slightly lower than the estimated EPMA analytical error. This indicates that more than 70 % of the clinopyroxene data are compositionally indistinguishable. The only part of the clinopyroxene Mg# distribution that is not fitted by the Gaussian distribution is a small shoulder at slightly higher Mg# values (76·1–78·3), which may indicate the presence of a few slightly more primitive clinopyroxene crystals. The lowest clinopyroxene Mg# values (<72·5) correspond to the most external few micrometers of crystal rims or to very small macrocrysts that perhaps belong to the groundmass. Clinopyroxene minor element concentrations are 1·2–3·4 wt% Al_2O_3 (mean = 2·30; $1\sigma = 0{\cdot}44$), 0·4–0·9 wt% TiO_2 (mean = 0·60; $1\sigma = 0{\cdot}09$), and 0·2–0·5 wt% Na_2O (mean = 0·32; $1\sigma = 0{\cdot}04$). Clinopyroxene trace element concentrations were measured in seven samples and show a restricted range. Except Cr, all elements above the detection limit show a coefficient of variation ($c_v = \sigma/\mu$, with μ the mean) below 0·2. The smallest c_v values are observed for REE (<0·15 for LREE and <0·10 for HREE). Clinopyroxenes are slightly to moderately enriched in REE (4·6–8·5 and 12–18 times Ce and Yb in CI chondrite, respectively; Fig. 10a), and have Ce/Yb ratios ranging from 1·22 to 1·79 and negative Eu anomalies (Eu/Eu* = 0·71–0·96).

Orthopyroxene major element compositions ($n = 1646$) were measured in 23 samples spanning the bulk-rock compositional range. Orthopyroxene Mg# ranges from 60·2 to 75·1 (mean = 69·3; $1\sigma = 4{\cdot}4$), a slightly larger range than previously reported by Morgado *et al.* (2019*a*) (66–71) and Arzilli *et al.* (2019)

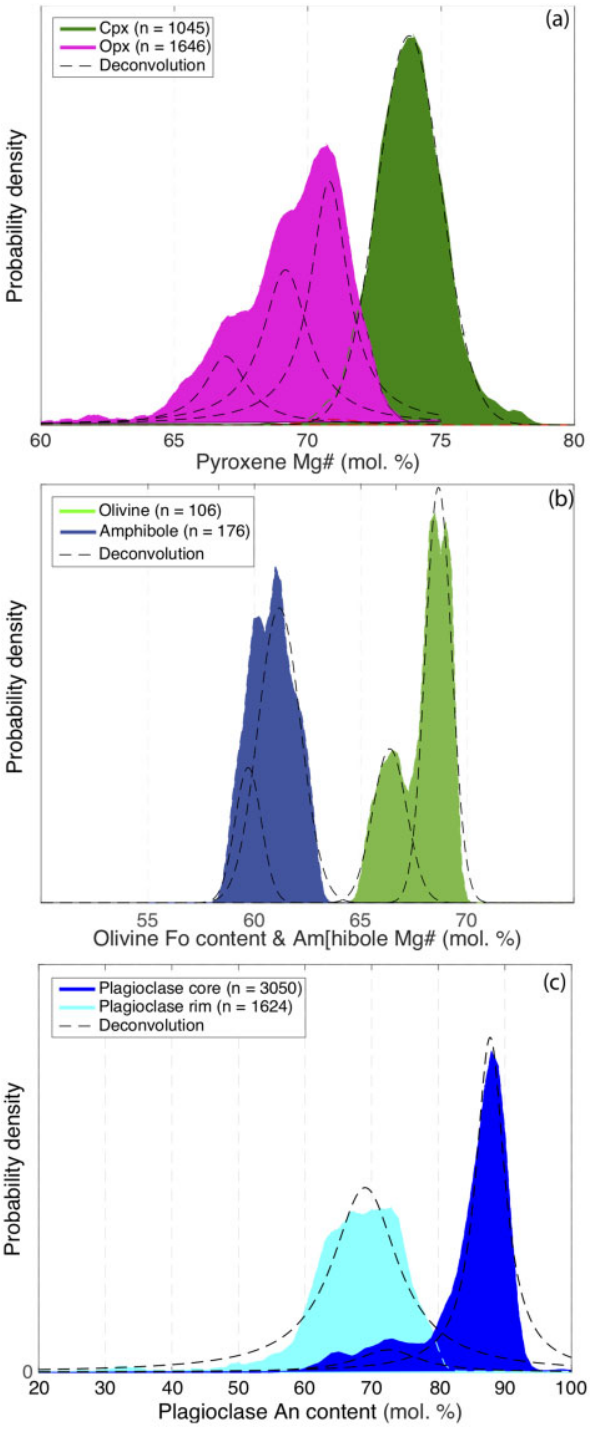

Fig. 9. Clinopyroxene, orthopyroxene, olivine, amphibole, and plagioclase major element compositions. (a) Density probability distribution of clinopyroxene and orthopyroxene Mg#. It should be noted that clinopyroxene data can be fitted by a single Gaussian distribution, whereas three Gaussian distributions are needed to fit the orthopyroxene data. Gaussian deconvolution was performed using a peak-fitting algorithm. (b) Density probability distribution of olivine Fo content and amphibole Mg#. (c) Density probability distribution of plagioclase anorthite (An) content. Cores and rims were distinguished by fitting an error function to individual core–rim compositional profiles [see details given by Namur *et al.* (2014)]. *n* is number of individual measurements.

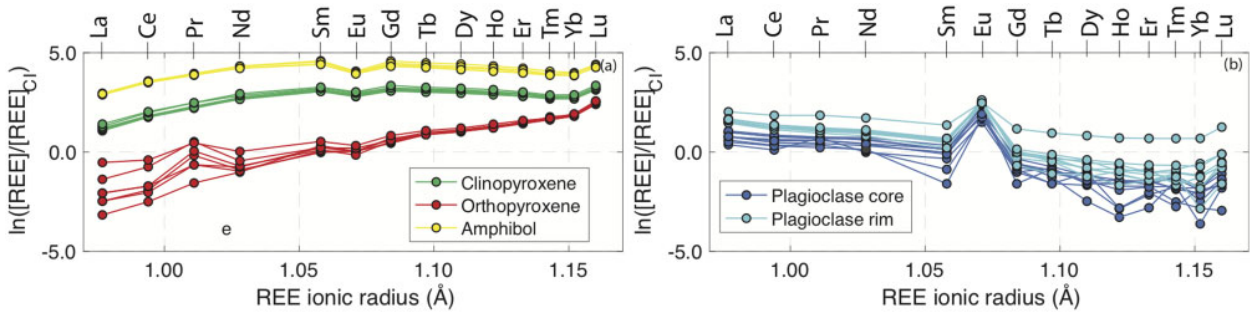

Fig. 10. REE concentrations in clinopyroxene, orthopyroxene, amphibole, and plagioclase. (a) Cl chondrite-normalized REE patterns of mafic mineral cores (concentrations plotted against ionic radius; O'Neill, 2016). (b) Cl-normalized REE patterns of plagioclase cores and rims.

(63–73). Our data were mostly collected along profiles. Eleven profiles in seven samples were successfully fitted with error functions. In those profiles, we observed a minor core–rim compositional contrast with the cores having Mg# values 2 mol% higher, on average, than those of the rims. Such normal zoning is subtle but visible in Fig. 2d. However, we stress that such a difference is only slightly higher than the estimated analytical error. For three other profiles, we did not obtain a good error function fit, but we observed some minor reverse zoning (up to 3 mol% Mg#), similar to those previously reported in samples from the 2015 eruption (Morgado *et al.*, 2019*a*). For all other profiles (73 profiles in 23 samples), we did not observe any statistically significant core–rim contrast, indicating that orthopyroxene is generally homogeneous at the crystal scale. At the eruption scale, the Mg# distribution of the full orthopyroxene dataset is largely unimodal, but cannot be adequately fitted by a single Gaussian distribution (Fig. 9a). We applied Gaussian deconvolution using the peakfit function of Matlab and iteratively increased the number of peaks until the goodness of the fit (root mean square deviation) stopped improving. We calculated that the data are best described by three Gaussian curves with medians at Mg# = 70·8, 69·2, and 66·9 (Fig. 9a). Although these values are not vastly different, they raise the possibility that three orthopyroxene populations exist in samples from the 2015 eruption. Again, some of the most evolved orthopyroxene compositions were measured in very small crystals straddling our arbitrary cut-off between microcryst and macrocryst, or even corresponding to microcrysts, and thus probably representing groundmass orthopyroxene. In addition, orthopyroxene replacing olivine in symplectites might be compositionally distinct from orthopyroxene macrocrysts. Orthopyroxene minor element concentrations are 0·5–2·2 wt% Al_2O_3 (mean = 1·16; 1σ = 0·37), 0·1–0·5 wt% TiO_2 (mean = 0·26; 1σ = 0·06), 1·2–2·2 wt% CaO (mean = 1·52; 1σ = 0·17), and 0·0–0·2 wt% Na_2O (mean = 0·07; 1σ = 0·03). Trace element concentrations measured in seven samples show a slightly larger compositional range than clinopyroxene. Except Sc, all elements above the detection limit show $c_v > 0·2$. The largest coefficients of variation (0·76–1·12) are observed for the lightest REE (La, Ce, Pr), although their concentrations are very close to the estimated detection limit (~0·01–0·03 ppm). Coefficients of variation are much smaller for HREE (0·20–0·29). Orthopyroxenes are depleted to slightly enriched in REE (i.e. 0·04–0·75 and 3·7–9·4 times Ce and Yb in Cl chondrite, respectively; Fig. 10a), and have large ranges of Ce/Yb ratios (0·04–0·37) and Eu anomalies (Eu/Eu* = 0·45–1·21) that are attributed to the large dispersion of the LREE data.

We observed cores of partly dissolved olivines in pyroxene crystals from at least 15 samples and measured their major element compositions (n = 106; Fig. 9b). The compositional variability of olivine is less than that of orthopyroxene and comparable with that of clinopyroxene. Olivine forsterite content [Fo = molar 100 × Mg/(Mg + Fe_t)] ranges from 65·2 to 71·1 (mean = 68·5; 1σ = 1·3), identical to that reported by Arzilli *et al.* (2019) but lower than that of Morgado *et al.* (2019*a*) (69–75). The bimodal distribution observed herein is best fitted by two Gaussian curves with a dominant median at $Fo_{68·7}$ and a minor shoulder at $Fo_{66·5}$. Olivine minor element contents are variable, with 0·07–0·21 wt% CaO (mean = 0·13; 1σ = 0·02) and 0·33–0·83 wt% MnO (mean = 0·53; 1σ = 0·09), which translates to tephroite contents [Tep = molar 100 × Mn/(Mg + Mn + Fe_t)] of 0·37–0·91. We did not measure trace elements in olivine.

As stated in the petrography section, amphibole was observed in a single sample (Supplementary Dataset 4). We measured core–rim profiles exclusively in tabular, euhedral crystals (n = 176). Amphibole is alkali-rich (Na_2O + K_2O = 2–3 wt%), relatively Al_2O_3-rich (9·05–10·57 wt%), and straddles the limit between pargasite and edenite following the classification of Leake *et al.* (1997). No obvious chemical variability is observed at the crystal or sample scale. Amphibole Mg# values are broadly unimodally distributed between 58·7 and 62·8 (mean = 60·8; 1σ = 0·94; Fig. 9b), slightly lower than the range reported by Morgado *et al.* (2019*a*) (64–77). Importantly, the crystal-scale variability (1σ of major element contents) is less than the standard deviations of experimental amphiboles reported by Ridolfi & Renzulli (2012). Amphibole crystals from Calbuco therefore do not show any obvious disequilibrium features and can be used for thermobarometric calculations (see

Discussion; Gorini *et al.*, 2018). Amphibole is fairly enriched in trace elements including LILE, HFSE, and transition metals, enriched in REE (33–36 and 47–54 times Ce and Yb in CI chondrite; Fig. 10a), and has high Ce/Yb ratios (2·3–2·6) and negative Eu anomalies (Eu/Eu* = 0·59–0·65).

Fe–Ti oxide compositions were obtained for nine samples ($n = 68$; Supplementary Dataset 4). According to our petrographic nomenclature, all measured Fe–Ti oxides are microcrysts, although they are markedly larger than typical matrix crystals. We observed abundant magnetite but no primary ilmenite crystals. Ilmenite was locally observed as micro-exsolutions in some magnetite grains, but the exsolutions were too small to be measured; we note, however, that Morgado *et al.* (2019*a*, 2019*b*) reported primary ilmenite crystals. Magnetite compositions are moderately TiO_2-rich (10·9–14·0 wt%), which translates to ulvöspinel (Usp) fractions of 0·30–0·42. The observed magnetite compositional distribution is best fitted by three independent distributions with median values at $Usp_{0.35}$, $Usp_{0.37}$, and $Usp_{0.41}$. This relatively small variability could indicate that we measured both phenocrysts smaller than 150 μm and groundmass crystals, or could result from sub-liquidus re-equilibration and ilmenite exsolution. We note that the magnetite compositional variability observed herein is lower than that described by Morgado *et al.* (2019*a*, 2019*b*), who reported low-Ti ($Usp_{0.10–0.17}$) and high-Ti magnetite populations ($Usp_{0.42–0.46}$). Minor element concentrations in magnetite are 2·1–4·0 wt% Al_2O_3 (mean = 3·5; $1\sigma = 0·30$), 1·6–4·9 wt% MgO (mean = 2·9; $1\sigma = 0·4$) and 0·24–0·55 wt% MnO (mean = 0·39; $1\sigma = 0·06$). We did not measure trace elements in magnetite.

Plagioclase

Plagioclase compositions were measured in 26 samples ($n = 4674$; Fig. 9c; average values for individual samples are reported in Supplementary Dataset 2). Most data were acquired along core–rim profiles. The majority of the profiles were successfully fitted with an error function, and, in those cases, we observed significant core–rim compositional contrasts but no intermediate mantle compositions. Some profiles did not show any inflection and may correspond to homogeneous grains with assumedly 'core' compositions or result from sectioning effects. To investigate plagioclase compositional variability at the eruption scale, we calculated probability density functions of plagioclase anorthite content [An = molar Ca/(Ca + Na)] for core and rim compositions separately. Plagioclase cores broadly have a median at $An_{86.8}$ and a median standard deviation of 5·1 mol%, although Gaussian deconvolution shows that the vast majority of the data is best explained by a Gaussian distribution with a median at $An_{87.7}$. The remaining cores are better explained by a second Gaussian distribution with a median at $An_{72.0}$ (Fig. 9c), which is only slightly more primitive than the median of the rim population ($An_{69.8}$; median standard deviation = 7·0 mol%). This indicates that the small population of data from unzoned crystals that we assumed to be evolved cores could instead correspond to plagioclase rim compositions. The rim population is well described by a single Gaussian distribution with a median at $An_{70.3}$ (Fig. 9c). Our median rim and core compositions are in agreement with previously reported compositional ranges from smaller sets of analyses (cores: $An_{78–93}$; rims: $An_{56–79}$; Arzilli *et al.*, 2019; Morgado *et al.*, 2019*a*). Such core–rim zonings are also observed in EDX maps obtained for some crystals (Fig. 11). Minor element concentrations are relatively similar in cores (0·02 ± 0·01 wt% TiO_2, 0·54 ± 0·10 wt% FeO) and rims (0·03 ± 0·02 wt% TiO_2, 0·55 ± 0·11 wt% FeO), except that K_2O slightly increases from 0·02 ± 0·01 wt% in cores to 0·06 ± 0·02 wt% in rims.

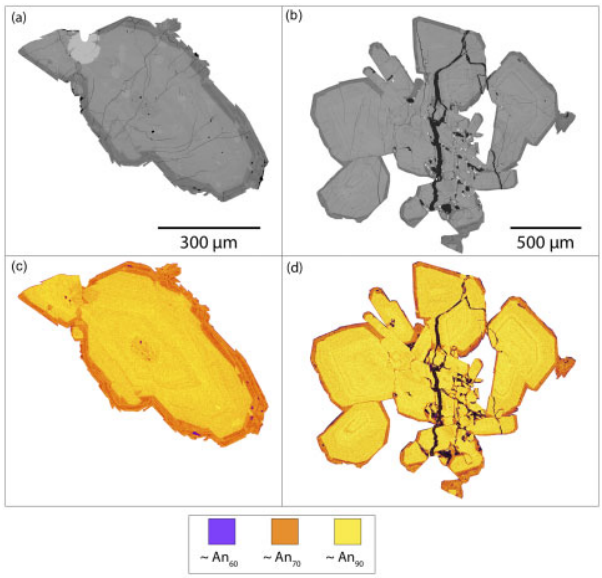

Fig. 11. Compositional features of representative plagioclase crystals. BSE images of (a) a representative plagioclase crystal and (b) a plagioclase-dominated glomerocryst. (c, d) False-colour Ca/(Ca + Na) EDX intensity maps of the same crystal and glomerocryst, respectively.

Trace element concentrations in plagioclase were measured in eight samples. Analyses were performed on cores and rims, which were optically discriminated using polarizing filters. Except for Sr and Ba (± Cr and V in some samples), all trace elements show very low concentrations (<3·8 ppm). Transition metals show standard deviations larger than their mean values, suggesting that mafic micro-inclusions were ablated during some measurements. Sr is the only compatible trace element in plagioclase, and its concentration does not change from core (637 ± 7 ppm) to rim (664 ± 17 ppm) ($\log E = 0·02$). In contrast, Ba concentrations increase significantly from core (16·7 ± 4·3 ppm) to rim (38·1 ± 5·7 ppm) ($\log E = 0·36$). We observe a significant bimodality among incompatible trace elements such as Rb, Y, and REE, with extremely low concentrations in

cores and higher concentrations in rims ($\log E = 0{\cdot}24$–$0{\cdot}61$). Of the REE, Eu shows the smallest degree of core–rim enrichment. REE are moderately depleted to moderately enriched (1·1–2·3 and 3·1–6·2 times Ce in CI chondrite in cores and rims, respectively; 0·13–0·17 and 0·16–1·98 times Yb in CI chondrite in cores and rims, respectively; Fig. 10b). Ce/Yb ratios are similar in cores and rims, although this is probably not meaningful because the extremely low Yb concentrations approach the detection limit. All plagioclase analyses show positive Eu anomalies that are almost identical in cores and rims ($Eu/Eu^* = 9{\cdot}94 \pm 3{\cdot}5$ and $9{\cdot}22 \pm 1{\cdot}93$, respectively).

DISCUSSION

Situating the 2015 eruption in the geochemical and mineralogical context of arc magmatism

We observed a series of important features in rocks from Calbuco, such as a high degree of crystallinity, the presence of zoned plagioclase crystals with highly calcic cores, and the presence of quenched glass that is significantly more evolved than the bulk-rock compositions. Whether these features have implications for a larger understanding of arc magmatism depends on how representative these samples are of arc magmas. We used Georoc to compile 61 000 bulk-rock data for all arcs worldwide (see complete list in Supplementary Data Fig. 3), the Andean arc, and the SVZ (details on data filtering and processing are provided in Appendix B). We note that Calbuco bulk-rock major oxide data are slightly displaced but within 1 MAD (median absolute deviation) of the median values of global arcs, the Andes, and the SVZ (Supplementary Data Fig. 3), and Calbuco bulk-rock compositions are particularly close to those of the SVZ. We also used Georoc to produce a filtered database of mineral compositions in arc magmas (see details in Appendix B). The modes of the orthopyroxene and clinopyroxene Mg# populations for the SVZ (71·0 and 72·3, respectively) are almost identical to the median values of Calbuco samples (69·7 and 73·8, respectively; Supplementary Data Fig. 4). Highly calcic plagioclase compositions ($An_{>80}$) as observed at Calbuco have been described in most arc segments, but are particularly common in the SVZ.

These results indicate that the geochemical and mineralogical features at Calbuco are highly relevant to arc volcanism, particularly in the SVZ. We therefore discuss the processes controlling the geochemical variability of Calbuco samples and the physico-chemical conditions under which the constituent minerals formed.

Mush crystals and the compositional variability of bulk-rock samples

It is commonly assumed that the eruption of multiple rock compositions from a single volcano broadly represents liquid compositions and defines a liquid line of descent from a single parental melt (e.g. Lee & Bachmann, 2014). When large databases are interrogated (Supplementary Data Fig. 3), it is striking that bulk-rock data at the scales of individual volcanoes, arc segments (e.g. SVZ), arcs (e.g. Andean), or global geodynamic settings (e.g. continental arcs) define coherent trends that are broadly reproduced by experimental phase relations or thermodynamic models. However, other processes such as variable degrees of melting of potentially contrasted mantle sources (Grove *et al.*, 2002), crustal assimilation (Hildreth & Moorbath, 1988), and magma (melt + crystal) mixing (e.g. Anderson, 1976; Murphy *et al.*, 1998; Browne *et al.*, 2006; Reubi & Blundy, 2009; Kent *et al.*, 2010) may contribute to geochemical diversity and produce compositional series that do not actually represent liquid lines of descent (Eichelberger, 1978; Eichelberger *et al.*, 2006). It is also recognized that lavas very commonly represent an assembly of various magmatic components, including melts and crystals that might originate from different parts of the magmatic system (e.g. Anderson, 1976; Neave *et al.*, 2014; Cashman *et al.*, 2017; Ganne *et al.*, 2018). Consequently, lavas may not directly represent liquid compositions, or if they do, they may not necessarily represent a single liquid line of descent (Eichelberger *et al.*, 2006). To obtain more detailed insight into subvolcanic processes, it is therefore useful to investigate the geochemical variability of individual eruptions.

Bulk-rock geochemical variability is usually small among eruptive products from a single eruption (Ruth *et al.*, 2016). When variable bulk-rock geochemical data are observed for a single eruption, they are usually attributed to the venting of a zoned magma chamber (Bacon & Druitt, 1988), the progressive mixing of various magma end-members during the course of an eruption (Ruprecht *et al.*, 2012; Higgins *et al.*, 2015), or the entrainment of crystals from a crystal mush prior to eruption (Ganne *et al.*, 2018). Morgado *et al.* (2019*a*) interpreted the high crystallinity of Calbuco samples and the presence of complex textural features in crystals as evidence for the presence of a crystal mush storage zone beneath Calbuco. Furthermore, the very strong and sharp compositional zoning of plagioclase crystals observed herein is inconsistent with closed-system fractionation; the absence of intermediate compositions between cores and rims indicates that these two zones crystallized in different environments and cannot have formed by continuous fractional crystallization. Therefore, the crystal cores most probably accumulated in a crystal mush before being mobilized and transported in the melt, at which time the rims crystallized (Costa *et al.*, 2010; Kent *et al.*, 2010; Neave *et al.*, 2014). Crystals with zoning patterns very similar to those observed at Calbuco have been described at other andesitic volcanoes (e.g. Mount St Helens, USA) and are interpreted as having crystallized in two steps: the cores crystallized first and resided in a relatively cold and deep part of the magmatic system before being entrained by a new batch of magma to a shallow

temporary storage region and, ultimately, to the Earth's surface (Cashman *et al.*, 2017).

Compared with global arc data, samples from the 2015 Calbuco eruption show a relatively small but significant range of bulk-rock compositions when compared with major elements such as SiO_2 (52·89–58·39 wt%; Figs 6 and 7) and MgO (2·51–5·61 wt%) or highly incompatible trace elements such as Zr (61–96 ppm; Fig. 8). The evolved compositions of these rocks preclude the hypothesis that they represent diverse primary melts (Wanke *et al.*, 2019). The restricted compositions of the glass phase among different samples also preclude progressive mixing of mafic and felsic liquid-dominated endmembers during the eruption (Higgins *et al.*, 2015). Fractional crystallization could potentially explain the geochemical diversity of the lavas, provided that each sample represents a different liquid composition, and that all samples derived from the same parental magma. Although we have no argument to fully exclude this process, we find it hard to reconcile with the restricted matrix glass geochemistry, which, in such a framework, would imply that all liquid compositions represented by individual samples experienced different degrees of *in situ* crystallization (Langmuir, 1989) or syn-eruptive decompression crystallization, yet produced a matrix melt of constant composition in all samples. This contrasts with the common observation that crystallization in a shallow magma chamber or during decompression produces moderate to large matrix glass compositional ranges (Cashman & Edmonds, 2019). Another argument suggesting that the observed bulk-rock variability does not arise from (fractional) crystallization is the absence of mineral compositional variability as a function of bulk-rock compositional indices such as SiO_2, which contrasts the continuous decrease of bulk-rock Mg# (i.e. proxy for pyroxene composition) and molar Ca/(Ca + Na) (a proxy for plagioclase composition) with increasing SiO_2 content. Although plagioclase composition may be influenced by changes in H_2O content during fractionation, a continuous decrease of bulk-rock Mg# would lead to significant pyroxene compositional variations if bulk-rock data directly represented melt compositions. However, although some compositional variability is observed in clinopyroxene and orthopyroxene, the average Mg# values of individual samples do not correlate with any bulk-rock differentiation index.

A simpler explanation of the bulk-rock variability at Calbuco is the venting of a magma chamber or a portion of the magmatic system containing a homogeneous dacitic melt, and the entrainment of mush crystals during eruption. However, we cannot exclude the possibility that the homogeneous matrix glass results from the efficient and rapid mixing of melt components originating from various depths in the crystal mush and of slightly different compositions (Namur & Humphreys, 2018). We note that, to some extent, crystal accumulation in a homogeneous melt may mimic a fractional crystallization trend if the mineral assemblage is of approximately cotectic proportions. Minerals in equilibrium with andesitic and dacitic melts are dominated by plagioclase, orthopyroxene, clinopyroxene, magnetite, ± olivine, ± amphibole (Botcharnikov *et al.*, 2008; Almeev *et al.*, 2013; Parat *et al.*, 2014), consistent with the mineral assemblage observed at Calbuco. Point-counting analyses indicate that the most typical mineral assemblage at Calbuco contains ~70 % plagioclase, 25–30 % pyroxene (clinopyroxene and orthopyroxene), and <5 % oxides (Supplementary Data Fig. 2), although point-counting data are based on individual thin sections or millimeter- to centimeter-scale lapilli, which notably may show small-scale heterogeneities (Ruth *et al.*, 2016).

We used bulk-rock, glass, and mineral major and trace element compositions to constrain the likely effect of mineral accumulation in a dacitic melt of composition identical to the average glass composition observed herein. We initially used principal component analysis to estimate the effect of mineral accumulation on bulk-rock chemistry (MacLennan *et al.*, 2001; Neave *et al.*, 2014). The first principal component (PC1) accounts for 91·06 % of the variability of important major element concentrations (SiO_2, Al_2O_3, FeO_t, MgO, and CaO; Supplementary Data Fig. 5). However, the coefficient of Al_2O_3 in PC1 is relatively low (0·13) owing to the absence of clearly evolving Al_2O_3 concentrations in the bulk-rock data (Fig. 6). Consequently, PC1 can be accounted for only by the addition or removal of dominantly mafic minerals, which contradicts our point-counting results that clearly indicate plagioclase as the major phase at Calbuco.

To estimate the extent to which mineral accumulation may affect bulk-rock geochemical variability, we evaluated the compositional evolution of a dacitic magma (again of Calbuco glass composition) when various proportions of crystals are accumulated (Passmore *et al.*, 2012). We considered mineral assemblages spanning the range of mineral modes observed in experiments on andesitic melts (Botcharnikov *et al.*, 2008; Almeev *et al.*, 2013; Parat *et al.*, 2014) and in Calbuco samples. These assemblages contain 50–90 wt% plagioclase and 10–50 wt% pyroxene (orthopyroxene and clinopyroxene). We neglected Fe–Ti oxides because we did not measure their trace element compositions and measured only the major element compositions of a few crystals. We started with a 50:50 plagioclase:pyroxene assemblage (clinopyroxene and orthopyroxene in identical proportions) and calculated how its accumulation by the melt affects bulk-rock major and trace element contents. The results for representative major and trace elements are plotted in Fig. 12 against SiO_2 or Zr content, and are compared with the linear regression on the bulk-rock data anchored on the average glass composition. The 50:50 plagioclase:pyroxene assemblage cannot reproduce our Calbuco bulk-rock data. We thus iteratively changed the mineral assemblage and minimized χ^2 between the mineral accumulation trend and the linear regression

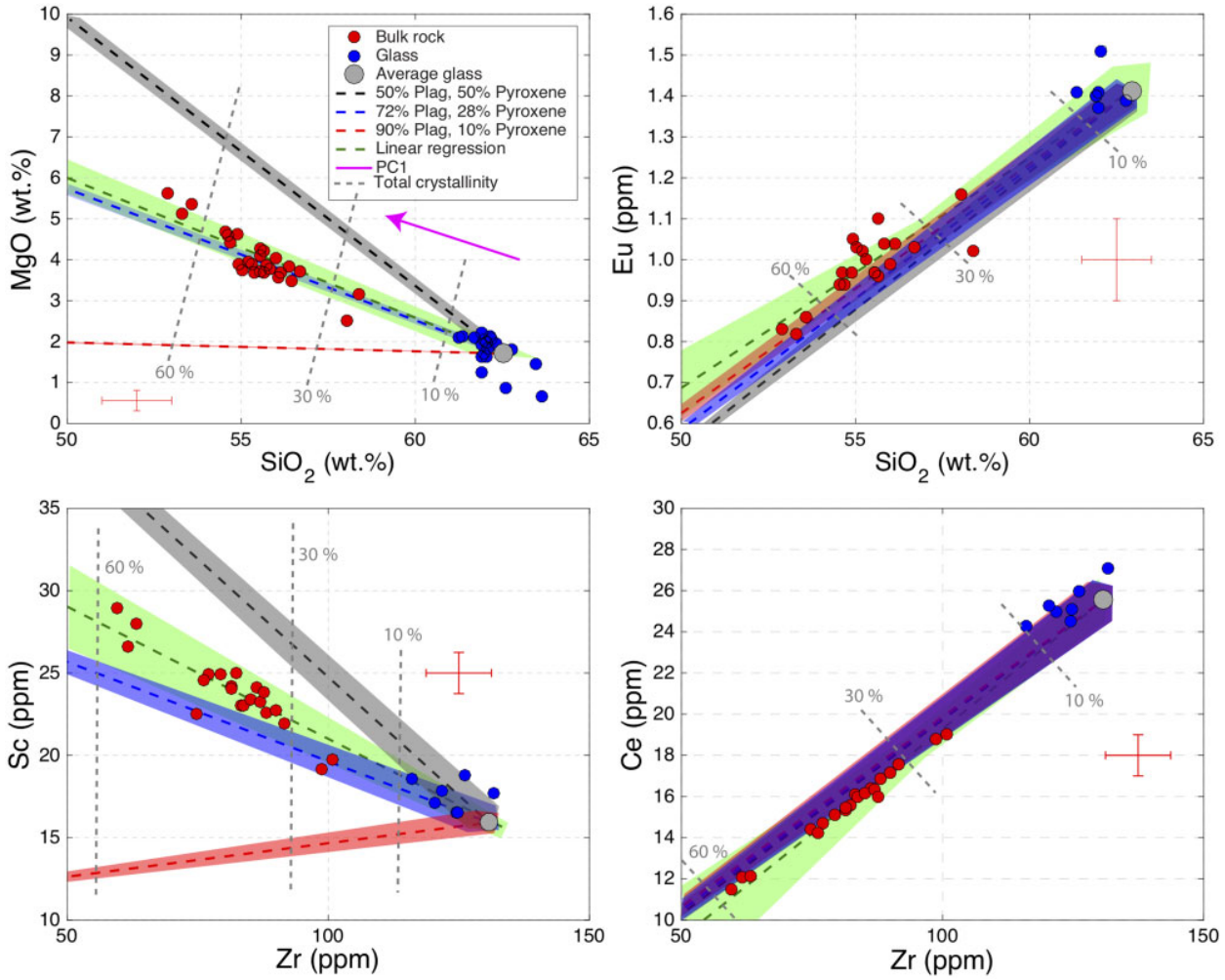

Fig. 12. Geochemical modelling of crystal accumulation. Geochemical effects of crystal accumulation (plagioclase, orthopyroxene, and clinopyroxene) in a dacitic melt. Modelling was performed for representative major (SiO_2, MgO) and trace elements (compatible: Sc; incompatible: Ce, Eu, Zr). Modelling results are compared with bulk-rock and data from 2015 Calbuco eruptive products (red and blue circles, respectively). We modelled the effect of incremental additions of 1% crystals in various mineralogical proportions using the average glass and crystal compositions. Grey, blue, and red envelopes account for 1σ errors on glass and mineral compositions. Green dashed lines are simple regressions through the bulk-rock and glass compositions, and green envelopes account for estimated analytical errors on the bulk-rock data (see red error bars). The cotectic proportions (blue dashed lines) were obtained through χ^2 minimization (i.e. minimization of the difference between modelling results and the linear regression through bulk-rock and glass compositions). The purple arrow is the projection of the first principal component (PC1) of bulk-rock data from principal component analysis, and the length of the arrow segment represents the 2σ error associated with PC1. The origin of the PC1 arrow is arbitrary.

on the bulk-rock. We performed this calculation for all major elements and compatible and incompatible trace elements. For most elements (except FeO_t and TiO_2), especially the most incompatible elements, 23–70 wt% accumulation of a 72:28 plagioclase:pyroxene assemblage (clinopyroxene and orthopyroxene in identical proportions) can reproduce the major and trace element compositions of our samples with a relative error of less than 10% (Fig. 12). For FeOt and TiO_2, a much better fit is obtained by adding 5% titanomagnetite. However, the flat Al_2O_3 trend cannot be reproduced by the simple accumulation of minerals in cotectic proportions, possibly indicating a slightly different plagioclase:pyroxene ratio in the various samples.

Based on our petrographic observations and the above geochemical modelling, we propose that the eruptive products of the 2015 Calbuco eruption represent the mobile part of a crystal mush that comprised dacitic melt and crystals dominated by plagioclase and pyroxenes. Although the co-eruption of melt and mush crystals has previously been described at arc volcanoes (Kent *et al.*, 2010) and in basaltic lavas (Passmore *et al.*, 2012; Neave *et al.*, 2014; Bennett *et al.*, 2019), the effect of crystal accumulation on bulk-rock chemistry has rarely been described (Neave *et al.*, 2014). Here, we have shown that the Calbuco andesites do not represent liquid compositions, but rather a mixture of minerals in cotectic proportions in a dacitic melt.

The dacitic glass matrix

A volumetrically important component of samples from the 2015 Calbuco eruption is the homogeneous dacitic matrix glass. Our 628 chemical analyses of quenched Calbuco glasses fall on the global geochemical trends observed for continental arc volcanoes. However, more than 85 % of glasses from other volcanoes are more evolved than Calbuco glasses (Supplementary Data Fig. 6), although we cannot exclude a sampling bias toward felsic compositions. To understand the origin of the dacitic melt and its link to the crystal cargo, we also compiled 1037 high-temperature experimental results from 41 studies performed at crustal pressure conditions (0·1–1300 MPa). We selected only experiments that contain melt, plagioclase, orthopyroxene, and clinopyroxene (i.e. the main phases observed at Calbuco) or that crystallize those phases along their liquid lines of descent. Liquids from 143 experiments are co-saturated with plagioclase, clinopyroxene, and orthopyroxene at 825–1230 °C and 0·1–1000 MPa. These liquids range in composition from basalt to rhyolite and contain 0–12 wt% H_2O, although about two-thirds of the liquids are andesitic ($n = 46$) or dacitic ($n = 47$). This suggests that the dacitic matrix observed at Calbuco could potentially be in equilibrium with its crystal cargo or could represent the residual melt after crystallization of those phases.

The most primitive magmas reported at Calbuco are basaltic andesites (~52 wt% SiO_2; 5–6 wt% MgO; Sellés *et al.*, 2004) that most probably derived from more magnesian parental melts (Grove *et al.*, 2003; Ulmer *et al.*, 2018). We therefore used rhyolite-MELTS (Gualda *et al.*, 2012) to calculate liquid lines of descent produced by fractional crystallization of primitive (Mg# > 65; 8–9 % MgO) basaltic andesites containing 0–3 wt% H_2O (as observed in basaltic andesites from nearby SVZ volcanoes; Watt *et al.*, 2013) (Fig. 13a). Our results indicate that the observed dacitic glass can be produced by 60 ± 8 % crystallization from a hydrous melt or ~50 % crystallization from a more evolved parental magma such as the Calbuco basaltic andesite (i.e. 5–6 wt% MgO) (Fig. 13b). For dry melts, 80 ± 5 % crystallization is required. These results are consistent with the calculations of Lee & Bachmann (2014) and reproduce relatively well the experimentally determined liquid lines of descent of high-Mg basaltic andesites and hydrous basalts (Grove *et al.*, 2003; Ulmer *et al.*, 2018).

The dacitic liquid at Calbuco was therefore most probably produced by the solidification of a parental basaltic andesite magma in a chamber that efficiently loses heat to its surroundings, producing crystal-rich mush systems over long timescales. At 50–70 % crystallinity, convective stirring stops and the physical segregation of the liquid from the crystals becomes efficient, periodically forming eruptible melt pockets of dacitic composition (Lee & Bachmann, 2014). Upon crystallization at crustal pressures, andesitic magmas may reach a pseudo-invariant point where the reaction hydrous melt + plagioclase + clinopyroxene + orthopyroxene = amphibole occurs (Blatter *et al.*, 2017). Amphibole crystallization at the peritectic point causes the system to dwell thermally owing to the peak of latent heat release (Ghiorso, 1997) under conditions producing dacite, strongly slowing crystallization and producing long-lasting pockets of very slowly evolving dacitic melt in crustal magma chambers. Because all our samples contain melt, plagioclase, and pyroxene, and one sample also contains amphibole, we suggest that the dacitic melt was extracted from a compositionally and thermally buffered amphibole-bearing crystal mush.

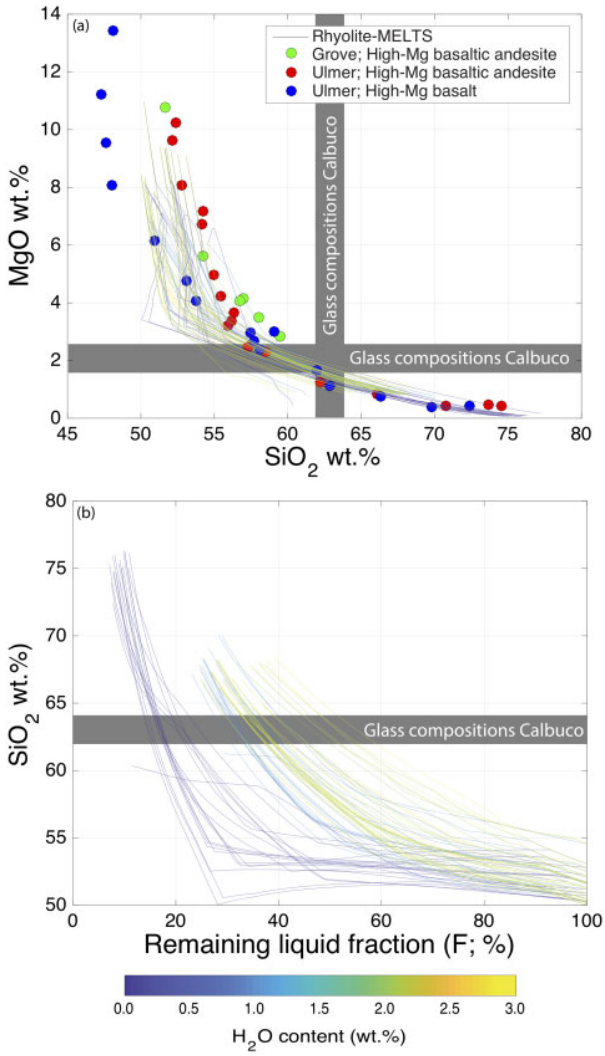

Fig. 13. Thermodynamic modelling of basaltic andesite differentiation. Geochemical modelling using rhyolite-MELTS (Gualda *et al.*, 2012) of the differentiation of primitive basaltic andesites (Mg# > 75) from the SVZ. Models were performed for initial H_2O contents (i.e. prior to crystallization) of 0–3 wt% in the parental magma. Results are compared with experimentally determined liquid lines of descent for high-Mg basaltic andesites and hydrous basalts (data points; Grove *et al.*, 2003; Ulmer *et al.*, 2018) and with dacitic glass compositions observed in 2015 Calbuco eruptive products (grey shaded areas).

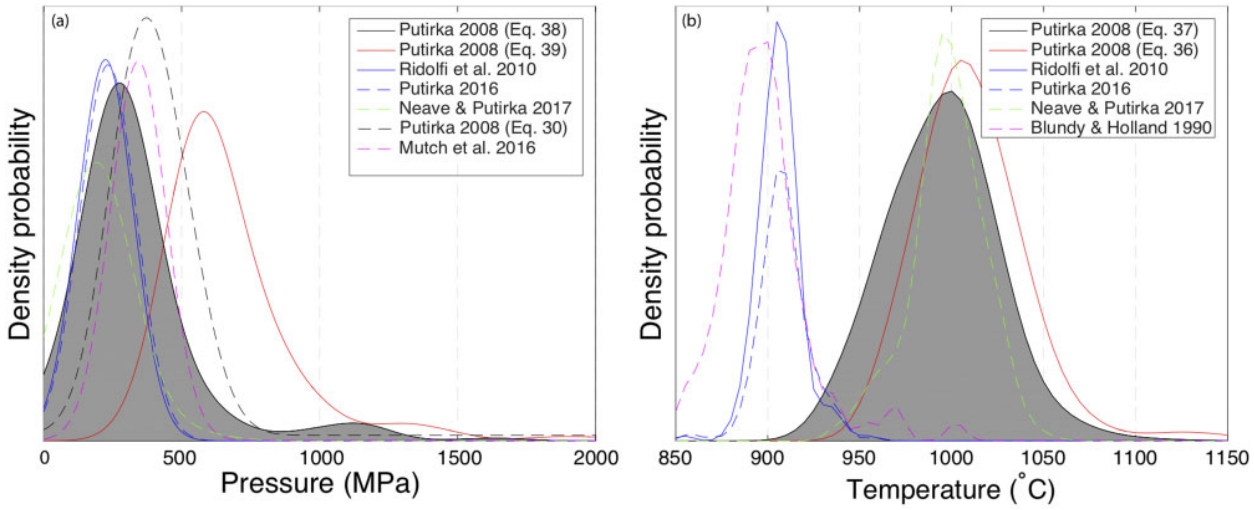

Fig. 14. Pressure–temperature estimates of crystal formation. (a) Pressure and (b) temperature estimates of pyroxene (orthopyroxene and clinopyroxene) and amphibole crystallization. (See text and Appendix C for details.)

Crystallization conditions

Pressure and temperature

Crystal transport in dacitic melt plays a major role in generating the observed geochemical diversity of Calbuco magmas. It is therefore crucial to estimate the crystallization conditions in order to reconstruct the volcano's plumbing system. Hence, we employed various geothermobarometers to investigate the crystallization conditions at Calbuco (Fig. 14).

We first investigated pyroxene crystallization using the two-pyroxene geothermobarometer [equations (36) and (37) of Putirka (2008); see details in Appendix C]. Both of the Putirka (2008) models produced consistent results, with a calculated temperature range between 919 and 1160 °C (mean = 1013 °C; 1σ = 39 °C; Fig. 14b). The standard deviation is comparable with the standard error of estimate (SEE) of the thermometer itself, indicating that the pyroxene population crystallized in a single, narrow temperature interval. Estimating clinopyroxene and orthopyroxene crystallization pressure is less straightforward because the two equations of Putirka (2008) give different results.

Putirka's equation (38) retrieves an almost normal distribution ranging from 0 to 2000 MPa (mean = 319 MPa; 1σ = 230 MPa), whereas his equation (39) retrieves a highly skewed distribution ranging from 300 to 2700 MPa (mean = 676 MPa; 1σ = 360 MPa).

The crustal thickness beneath Calbuco is ~30–32 km (Tasarova, 2007; Syracuse *et al.*, 2010; Dzierma *et al.*, 2012). Considering an average crustal density of 2800 kg m^{-3} (Weidmann *et al.*, 2013), this crustal thickness translates to a pressure at the Moho of 880 MPa. Because more than 25% of the pressure estimates obtained using equation (39) of Putirka (2008) exceed the pressure at the Moho, we consider the results obtained using his equation (38) to be more realistic, and suggest that pyroxene crystallization occurred at 319 ± 230 MPa, corresponding to 11·6 ± 8·4 km depth. Because the variation of the pressure estimates is similar to the error of the model, all pyroxenes most probably formed in a single storage region or a series of sill-like chambers at ~11·6 km depth.

Pressure and temperature conditions in magmatic systems can also be estimated from clinopyroxene–melt equilibrium. We used the model of Neave & Putirka (2017). (See Appendix C for details.) We obtained pressure estimates between 0 and 710 MPa (mean = 200 MPa, equivalent to 7·2 km depth; 1σ = 95 MPa). These values are slightly lower than those obtained with the older clinopyroxene–liquid model [equation (30) of Putirka, 2008; 120–810 MPa; mean = 380 MPa; 1σ = 92 MPa], but are comparable, within errors, with those obtained with the two-pyroxene barometer of Putirka (2008). To estimate temperatures, we used the thermometer of Neave & Putirka (2017) [based on equation (30) of Putirka, 2008; see details in Appendix C]. Considering 3 wt% H_2O in the melt, we obtained temperature estimates from 924 to 1067 °C (mean = 997 °C; 1σ = 20 °C); estimated temperatures are ~20 °C lower when considering 4 wt% H_2O in the melt. These values are almost identical to those obtained with the two-pyroxene thermometer (Fig. 14b).

The presence of amphibole in one sample can be used to further constrain the Calbuco plumbing system. We used the expression of Ridolfi *et al.* (2010) to obtain pressure and temperature estimates for each EPMA analysis of amphibole. The accuracy of this expression has been discussed in the literature (Erdmann *et al.*, 2014), but it should be accurate for Calbuco amphiboles containing >9 wt% Al_2O_3 (Gorini *et al.*, 2018). We obtained 176 pressure and temperature estimates defining normal distributions around 906 °C (1σ = 12 °C) and 224 MPa (1σ = 14 MPa). Identical results were obtained with the more recent model of Ridolfi & Renzulli (2012), whereas the Al-in-hornblende barometer of Mutch *et al.*

(2016) returned slightly higher pressure conditions (338 MPa; $1\sigma = 18$ MPa). Although calibrated using andesitic compositions, this last model might be more accurate for highly silicic systems. Our estimates are also similar to those of Morgado *et al.* (2019*a*), which were obtained using the expression of Ridolfi *et al.* (2010). We also estimated amphibole crystallization conditions using the amphibole–melt thermobarometric equation of Putirka (2016). For the melt component, we used the average glass composition of the glass-bearing samples. The average $K_{amp\text{-}liq}^{(Fe\text{–}Mg)}$ value of the amphibole–liquid pairs is 0·273, indicating that both phases are in chemical equilibrium. Pressure and temperature estimates obtained with the amphibole–melt thermobarometer are almost identical to those obtained using the expression of Ridolfi *et al.* (2010), and the temperature estimates are similar to those obtained with the plagioclase–amphibole thermometer (898 °C; $1\sigma = 24$ °C; Blundy & Holland, 1990). The amphibole crystallization pressure is well constrained by all models and is relatively similar to that obtained for pyroxene crystallization. The lower temperature of amphibole crystallization compared with that of pyroxenes, however, indicates that amphibole is a later-crystallizing phase in Calbuco magmas, in agreement with experimental results (Almeev *et al.*, 2013; Parat *et al.*, 2014). Finally, we note that the magma storage pressure obtained in this and previous studies (Arzilli *et al.*, 2019; Morgado *et al.*, 2019*a*) translates to a depth similar to the estimated source of co-eruptive deflation (8–11 km; 220–300 MPa; Delgado *et al.* 2017) and is similar to that estimated for the main storage region below the nearby La Picada volcano (Vander Auwera *et al.*, 2019).

The formation of plagioclase cores

Highly anorthitic plagioclase cores are an important component of the magma erupted during the 2015 Calbuco eruption. By combining our EPMA and EDX data (Figs 9c and 10) with BSE images of plagioclase macrocrysts and microcrysts (Fig. 3), we can better understand the CSDs reported in Fig. 5. Our results suggest that plagioclase crystals with high-An cores and more albitic rims form the population of large crystals ($A^{0.5} > 500\,\mu m$) whereas evolved microcrysts form the population of small crystals ($A^{0.5} < 500\,\mu m$). The very strong and sharp zoning between cores and rims in the population of large plagioclases clearly indicates that the cores are in thermodynamic disequilibrium with the melt (glass) in which they are found. Such a disequilibrium between cores and the carrier liquid was suggested by Morgado *et al.* (2019*a*) based on MELTS modelling (Ghiorso & Sack, 1995) showing that only plagioclase rim compositions can crystallize from the carrier melt.

The origin of high-CaO plagioclase has been investigated in the contexts of subduction zone (Couch *et al.*, 2003; Hamada *et al.*, 2011; Kemner *et al.*, 2015; Melekhova *et al.*, 2017) and mid-ocean ridge volcanism (Panjasawatwong *et al.*, 1995; Kohut & Nielsen, 2003; Drignon *et al.*, 2018). Experimental investigations have illustrated the dominant role of melt CaO/Na_2O ratio and H_2O content in equilibrium plagioclase An content (Sisson & Grove, 1993; Panjasawatwong *et al.*, 1995). Arzilli *et al.* (2019) presented H_2O measurements of melt pockets referred to as plagioclase-hosted melt inclusions, but did not provide locations of these melt pockets within the crystal (i.e. within An-rich cores or more albitic rims). It is also unclear if their data represent initial melt H_2O contents or were affected by post-entrapment crystallization (Neave *et al.*, 2017*b*). Based on their H_2O concentration data and rhyolite-MELTS modelling (Gualda *et al.*, 2012), Arzilli *et al.* (2019) proposed that plagioclase cores in Calbuco formed after 10–15 % crystallization of a basaltic andesite magma (average bulk-rock concentration of eight samples from the 2015 eruption) at ~300 MPa, and that further 10–25 % crystallization produced the albitic rims. However, this model is inconsistent with the very sharp compositional contrast observed herein between plagioclase cores and rims, which cannot be explained by the continuous fractional crystallization of a single parental melt.

To estimate the melt composition that might have crystallized the anorthitic cores, we compiled an experimental dataset (1742 experiments from 77 studies) containing melts ranging from basalt to rhyolite (43–75 wt% SiO_2; 0–11 wt% MgO) with a large range of H_2O contents (0–16 wt%; measured or estimated as 100 % – sum of oxides). Most plagioclase crystal cores at Calbuco are $An_{>85}$. In the experimental database, only two liquid compositions are in equilibrium with such anorthitic plagioclase, both being H_2O-rich (>3 wt%) basalts (<50 wt% SiO_2) that are compositionally very different compared with Calbuco bulk-rock data. Only a few intermediate liquid compositions (>50 wt% SiO_2) similar to Calbuco bulk-rock data are in equilibrium with $An_{>80}$, but all these melts are highly enriched in water (6–13 wt% H_2O).

One common hypothesis for the formation of high-An plagioclase is crystallization from refractory melts with very high CaO/Na_2O ratios (Panjasawatwong *et al.*, 1995). By extrapolation of the main experimental trend in our compilation, we speculate that dry melts would require very large CaO/Na_2O ratios (>10–15) to produce plagioclase with $An_{>85}$ (Supplementary Data Fig. 7). Such ratios have not been observed in the SVZ [mean = 1·96, p90 = 4·16, mean(Mg# > 70) = 3·21; where p90 is the 90th percentile and mean(Mg# > 70) corresponds to the mean CaO/Na_2O ratio of magmas with Mg# > 70], in global arc systems [mean = 2·22; p90 = 4·43; mean(Mg# > 70) = 3·96], nor in plagioclase- or olivine-hosted melt inclusions [mean = 2·18; p90 = 5·15; mean(Mg# > 70) = 5·47]. It is highly unlikely that the extremely common high-An plagioclase cores in SVZ lavas crystallized from melt compositions that have never been observed in bulk-rock or glass compositional data. A recent study of plagioclase-ultraphyric basalts from the Blanco

transform fault (offshore Oregon, USA) suggested that anorthitic plagioclase might have crystallized in the mantle (Drignon *et al.*, 2018), perhaps from a refractory melt that reacted with the Al-spinel-bearing upper mantle (Kohut & Nielsen, 2003). However, high-MgO andesites or boninites in equilibrium with a lherzolitic source rarely have CaO/Na_2O ratios exceeding 5–6 (Sobolev & Danyushevsky, 1994; Grove *et al.*, 2003). It is therefore also highly unlikely that the high-An plagioclase cores at Calbuco crystallized in the mantle, and we rather consider that melt H_2O content must have played a major role in the formation of high-An plagioclase cores.

The presence of amphibole in one Calbuco sample indicates the presence of water in these magmas. Recent estimates of H_2O contents in plagioclase- and pyroxene-hosted melt inclusions suggest that Calbuco magmas could contain 2–7 wt% H_2O (Arzilli *et al.*, 2019). Although Arzilli *et al.* did not specify the positions of the inclusions within the plagioclase crystals, their data indicate that high-An plagioclase, the most primitive phase observed at Calbuco, may have crystallized from a moderately to strongly H_2O-enriched magma. Because amphibole appears in upper crustal (~200 MPa) andesitic melts only when the melt H_2O content reaches 4–6 wt% (Parat *et al.*, 2014), and because amphibole crystallizes much later than An-rich plagioclase cores at Calbuco, it is unlikely that An-rich plagioclase crystallized from a melt containing significantly more than 4 wt% H_2O. To test the effect of H_2O on plagioclase anorthite content, we performed thermodynamic simulations using MELTS. We automatically performed series of batch calculations (i.e. Jennings & Holland, 2015; Namur *et al.*, 2016) for 4350 bulk-rock compositions from the SVZ containing 1 or 4 wt% H_2O and calculated the composition of the first plagioclase that saturates at 250 MPa along their liquid lines of descent. Our results indicate that SVZ magmas containing 1 wt% H_2O crystallize plagioclase with $An_{20–82}$ (median = An_{70}, mode = An_{77}; Fig. 15a), compositions matching the Calbuco plagioclase rims, not cores. Increasing the melt water content to 4 wt% H_2O increases the plagioclase An content to $An_{30–93}$ (median = An_{78}, mode = An_{82}), although perhaps not sufficiently to explain the observed core compositions (median = An_{87}, mode = An_{87}; Fig. 15b).

To better constrain the formation conditions of the highly anorthitic plagioclase cores, we conducted further modelling using a recently calibrated plagioclase–liquid hygrometer designed to calculate the water content of a melt in equilibrium with plagioclase based on melt composition, plagioclase An content, and temperature (Waters & Lange, 2015). We reformulated the expression of Waters & Lange to output the equilibrium plagioclase composition (An content; See details in Appendix D).

The results of our calculations show that highly anorthitic plagioclase similar to the cores observed in Calbuco rocks ($An_{82–92}$) can theoretically be produced by a range of melt compositions containing 1–8 wt% H_2O (Fig. 16a). The major element compositions of these melts span highly refractory, primitive basalt (45 wt% SiO_2; 10 wt% MgO) to evolved dacite (65 wt% SiO_2; 1 wt% MgO; Fig. 16b). Within the bulk-rock compositional spectrum of the SVZ, the most common magma capable of crystallizing high-An plagioclase cores corresponds to a basaltic andesite with ~52 wt% SiO_2, 5–6 wt% MgO, and CaO/Na_2O = 1·8–3·5. This composition exactly falls on the predicted liquid lines of descent of the most primitive magma compositions described at Calbuco (Fig. 13). For such a melt to produce the observed plagioclase core compositions ($An_{82–92}$) requires 3·5–4·5 wt% H_2O and a liquidus temperature of ~1050 °C. This temperature is in perfect agreement with experiments on fluid-saturated basaltic

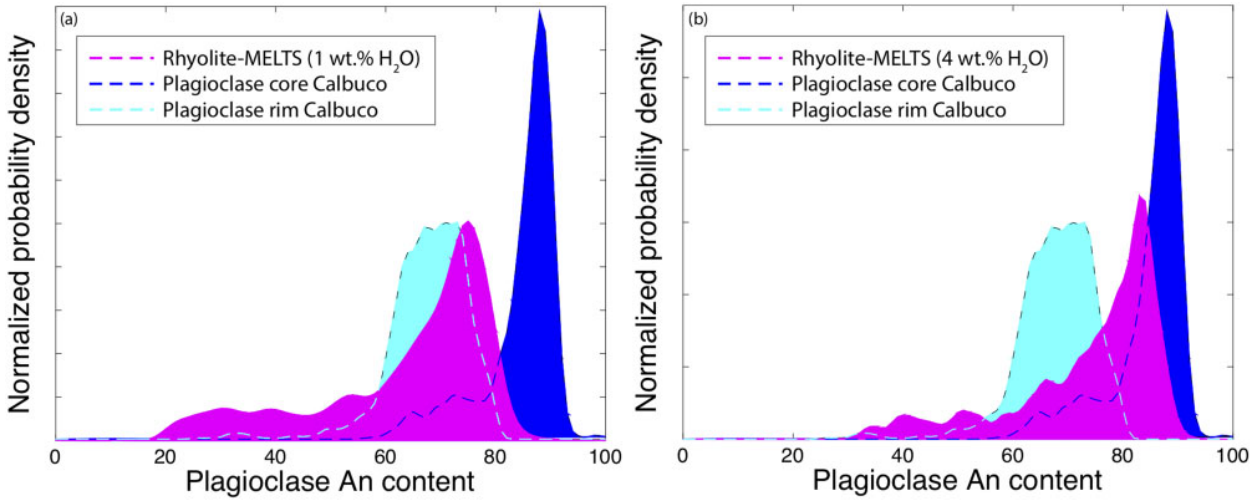

Fig. 15. Thermodynamic modelling of plagioclase compositions. Geochemical modelling using rhyolite-MELTS (Gualda *et al.*, 2012) of the plagioclase composition at plagioclase saturation for 4350 bulk-rock compositions from the SVZ. Calculations were performed with (a) 1 wt% and (b) 4 wt% H_2O in the parental melt. Model results are compared with plagioclase core and rim compositions observed in the 2015 Calbuco eruptive products.

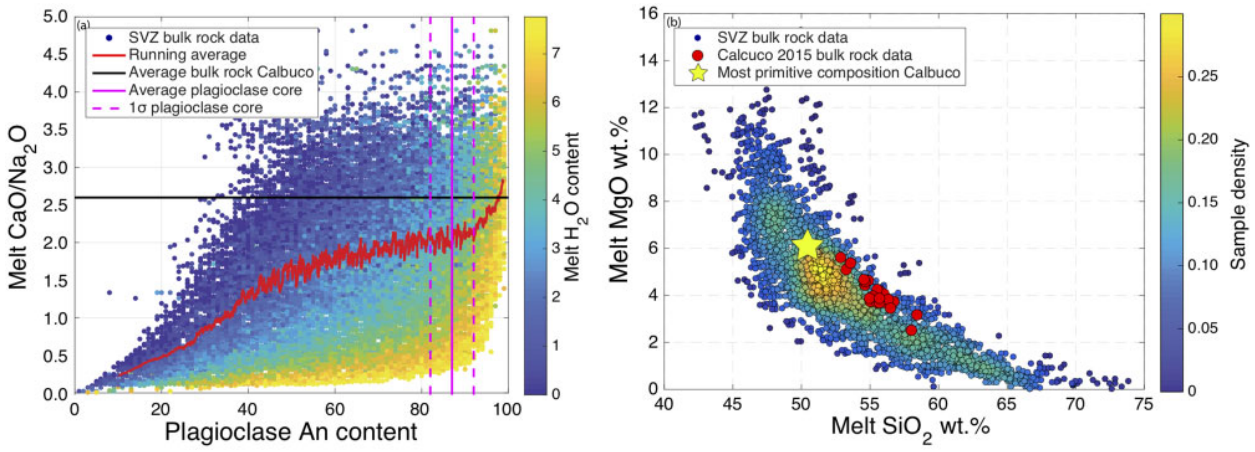

Fig. 16. Parental melts of plagioclase cores. (a) The relationship between melt CaO/Na_2O ratio and the equilibrium plagioclase composition as a function of melt H_2O content. We used a modified version of the hygrometer equation of Waters & Lange (2015) to calculate plagioclase An content. The starting compositions of the calculation correspond to 4350 bulk-rock compositions from the SVZ. The liquidus temperature for each magma was estimated using the geothermometer shown in Supplementary Data Fig. 8. The horizontal black line represents the average CaO/Na_2O ratio of the magma erupted during the 2015 Calbuco eruption, and the vertical pink lines represent the average ($\pm 1\sigma$) composition of plagioclase cores. It should be noted that the running average crosses the vertical continuous pink line at a melt H_2O content of ~4–4·5 wt%. (b) Density plot showing the range of magma compositions (MgO vs SiO_2, wt%) capable of crystallizing the plagioclase cores observed in 2015 Calbuco eruptive products. It should be noted that the highest density corresponds to basaltic andesites with a composition almost identical to the most primitive composition observed at Calbuco (Sellés *et al.*, 2004). Bulk-rock compositions of samples from the 2015 Calbuco eruption are shown for reference.

andesites similar to those observed at Calbuco (Moore & Carmichael, 1998; Almeev *et al.*, 2013; Parat *et al.*, 2014), which very commonly contain plagioclase with An contents above 80, and often approaching 85. Our estimated H_2O contents are also in agreement with those observed in parental melts at nearby volcanoes (Watt *et al.*, 2013). An alternative parental magma composition for the high-An cores could be an evolved andesite (e.g. ~58 wt% SiO_2), similar to the most primitive plagioclase-hosted inclusions described by Arzilli *et al.* (2019), with 6·0–6·5 wt% H_2O. However, we exclude this hypothesis because amphibole would be a liquidus phase well before the appearance of plagioclase and before olivine reacts to orthopyroxene in such a hydrous melt, which is inconsistent with the abundant glomerocrysts comprising An-rich plagioclase, pyroxene, and olivine (reacted to orthopyroxene), but no amphibole in Calbuco rocks. Indeed, the absence of amphibole and the presence of reacted olivine in the glomerocrysts indicate that An-rich plagioclase and pyroxenes crystallized from a melt containing <5 wt% H_2O (Botcharnikov *et al.*, 2008; Parat *et al.*, 2014), in agreement with the very low fraction of amphibole observed in 2015 Calbuco eruptive products. The minor influence of amphibole fractionation on the 2015 Calbuco magmas is further supported by the relatively constant Dy/Yb and Dy/Dy* values (Davidson *et al.*, 2013; where $Dy* = La_N^{4/13}Yb_N^{9/13}$; Supplementary Data Fig. 9) observed in all but the two most silicic samples that are not representative of 2015 Calbuco eruptive products.

We therefore propose that the An-rich cores observed at Calbuco crystallized in a magma chamber at 200–300 MPa and represent the crystallization products of a primitive basaltic andesite similar to those described for previous Calbuco eruptions (Sellés *et al.*, 2004). As previously suggested for Calbuco (Morgado *et al.*, 2019*a*) and many other volcanoes in both convergent and divergent settings (Costa *et al.*, 2010; Druitt *et al.*, 2012; Passmore *et al.*, 2012; Neave *et al.*, 2014; Ruth *et al.*, 2016), these crystals most probably accumulated to form a crystal mush along with co-crystallized olivine and possibly pyroxenes. This hypothesis is in agreement with the average SiO_2 content of olivine-hosted melt inclusions, although pyroxene-hosted inclusions are more evolved (Fig. 6).

A pre-eruptive model for Calbuco

The lack of precursory signals before the 2015 Calbuco eruption (Arzilli *et al.*, 2019; Morgado *et al.*, 2019*a*) has led some researchers to consider that there was no magma movement beneath the volcano in the months to years before the eruption (Arzilli *et al.*, 2019). However, this contradicts the increased seismicity observed during the several months prior to the eruption (Castruccio *et al.*, 2016; Romero *et al.*, 2016), in particular a VT event of local magnitude 3·0 recorded at 16 km depth beneath the volcano on 27 May 2014 and the continuous increase of VT seismicity during the 3 months leading up to the eruption (although the number of events remained relatively low at 40–60 VT events per month). Assuming no magma movement prior to the 2015 eruption, Arzilli *et al.* (2019) proposed a pre-eruptive model in which a basaltic andesite was emplaced at 200–300 MPa, cooled, and initially crystallized An-rich plagioclase (and presumably some mafic

minerals). Further crystallization of groundmass crystals and plagioclase rims would have led to fluid saturation followed by over-pressurization in the magma chamber and, ultimately, eruption. However, this model cannot explain the very sharp compositional contrast between plagioclase cores and rims, which implies that plagioclase rims did not form as the simple differentiation product of the same melt that crystallized the plagioclase cores, or at least not under the same equilibration (pressure) conditions.

Here, we propose an alternative pre-eruptive model that acknowledges both the minor tectonic events that occurred before the 2015 eruption and the highly zoned plagioclase crystals that record crystallization in different environments (Cashman *et al.*, 2017). Indeed, different crystallization environments, or at least a mixture of crystal populations, are also required to explain the kinked plagioclase CSDs (Fig. 5) and perhaps the minor spread among pressure conditions calculated with different geobarometers. We propose that a basaltic andesite with an initial H_2O content of 3–4 wt% and a liquidus temperature of ~1050 °C was emplaced at <300 MPa beneath Calbuco (Fig. 17). Plagioclase and olivine were the first phases to crystallize. The moderately high melt H_2O content and the relatively low pressure of the magma chamber led to the formation of highly anorthitic plagioclase (Longhi *et al.*, 1993; Sisson & Grove, 1993). Upon cooling to about 30–40 °C below the liquidus, olivine reacted out and mafic phases were dominated by orthopyroxene and clinopyroxene (Botcharnikov *et al.*, 2008). According to our estimates and experimental studies, these phases crystallized at ~1000 °C (Fig. 14). During this crystallization interval, the melt fraction decreased by 40–50 %, as estimated from *rhyolite-MELTS* calculations and experimental studies (Moore & Carmichael, 1998; Almeev *et al.*, 2013). The increasing melt H_2O content during crystallization opposed the effect of fractional crystallization

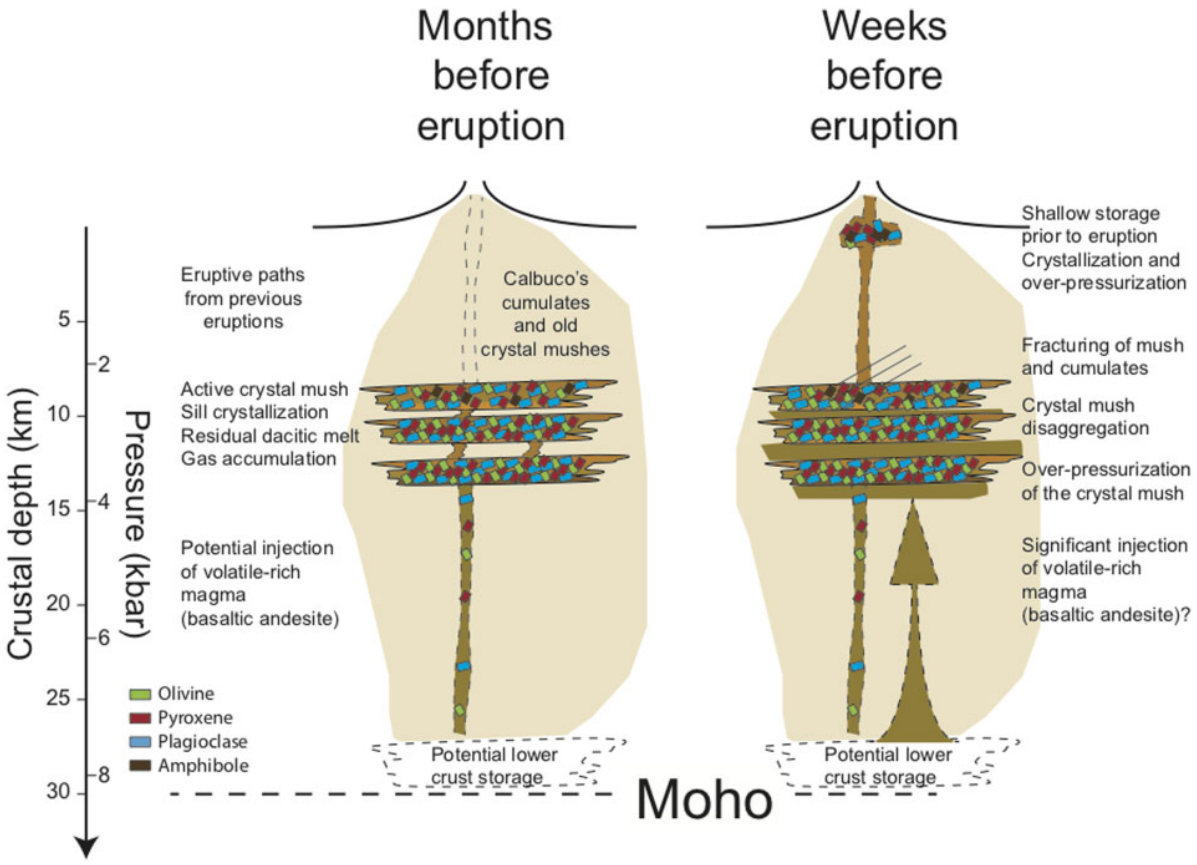

Fig. 17. Schematic pre-eruptive diagram of the plumbing system at Calbuco. Years to months prior to the 2015 eruption, primary melt formed in the mantle differentiated (possibly at lower-crustal storage conditions) and accumulated in mid-crustal sills (~300 ± 200 MPa). Crystallization led to the formation of a crystal mush dominated by melt, anorthitic plagioclase, and olivine, and further crystallization led to the appearance of clinopyroxene, orthopyroxene, and eventually amphibole. At the appearance of amphibole (i.e. after ~60 % crystallization), the residual melt evolved to a dacitic composition. A few months to weeks before the 2015 eruption, the top of the mid-crustal crystal mush became disaggregated and migrated to a shallow storage region owing to either a significant injection of primitive melt at the bottom of the mid-crustal storage region or over-pressurization of the magma reservoir. Further crystallization of the dacitic melt in the shallow storage regions led to the formation of evolved (relatively albitic) plagioclase rims and individual smaller crystals, and perhaps minor normal zoning in mafic phases. The combined effects of crystallization and the low pressure of the shallow magma storage region resulted in over-pressurization of the shallow magma chamber, which triggered the April 2015 eruption.

on plagioclase An content, which remained constant or perhaps even slightly increased (Botcharnikov *et al.*, 2008; Almeev *et al.*, 2013), possibly explaining the minor chemical variability observed in plagioclase cores (Fig. 3e). Although we cannot determine whether fluid saturation was reached at this stage, we suggest that, at fluid saturation (>7–8 wt% H_2O; Moore & Carmichael 1998), the fluid phase must have accumulated in the plumbing system because no passive degassing was observed before the eruption.

The presence of 50–250 μm wide relatively An-poor rims on plagioclase crystals and the complete absence of intermediate compositions between the cores (average An_{87}) and rims (average An_{70}) indicate that the conditions of magma crystallization suddenly and drastically changed at some point during differentiation, and that the crystals were transported to one or more different storage regions. Our plagioclase trace element profiles are not at sufficient spatial resolution to accurately model diffusion and estimate magma transport and accumulation timescales. Nonetheless, based on experiments simulating the growth of relatively An-poor plagioclase on An-rich seeds (average growth rate 30×10^{-10} cm s^{-1}; Larsen, 2005), we suspect that the crystallization conditions must have changed about 2 months to 1 year before eruption, although plagioclase growth rates of the order of 10^{-9}–10^{-11} cm s^{-1} reported for other shallow volcanic systems (Cashman, 1993; Turner *et al.*, 2003; Larsen, 2005; Pupier *et al.*, 2008) lead to timescales of days to years. Our rough estimate is, however, of the order of other estimates based on diffusion modelling of natural samples with similar rim sizes (about 2 years; Izbekov *et al.*, 2002; Druitt *et al.*, 2012) and is identical to the residence time of blocky microlites observed at Calbuco (Arzilli *et al.*, 2019). It also roughly corresponds to the first VT events observed before the 2015 eruption.

Based on findings from a detailed melt inclusion study of Llaima (Ruth *et al.*, 2016), a nearby volcano in the SVZ, we tentatively suggest that the top of the crystal mush or a crystal-rich melt-dominated pocket within a long-lasting magma chamber (perhaps several kilometers thick) suddenly moved to a very shallow storage region or possibly into the edifice and conduit system (Fig. 17). At Llaima, it was shown that such a shallow chamber formed at 25–100 MPa, corresponding to 1–4 km depth. Some plagioclase-hosted melt inclusions measured by Arzilli *et al.* (2019) contain <2 wt% H_2O, perhaps also suggesting a final equilibration at low pressure (<50 MPa). Crystals transported from the mid-crustal to the shallow storage region are represented by the population of larger plagioclase crystals and mafic minerals, and our modelling suggests that plagioclase and pyroxene were transported in nearly cotectic proportions. The very low amount of olivine observed in the 2015 eruptive products may be due to efficient grain dissolution prior to crystal mush rejuvenation or unlocking of the layered crystal mush (Neave *et al.*, 2014), the latter being in agreement with the occurrence of some ultramafic glomerocrysts in Calbuco rocks. Crystal transport between storage regions can also explain the minor dissolution features observed in plagioclase crystals (Nelson & Montana, 1992), and may have further contributed to olivine dissolution.

Two mechanisms might explain the migration of a crystal-rich magma to a shallower storage region. (1) Local fluid saturation and over-pressurization in the deeper part of the crystal mush, where the melt composition is likely to be very evolved, might cause fracturing in the rheologically locked and highly crystalline part of the magma chamber and overlying country rocks (Huber *et al.*, 2011), which may lead to upward migration of crystals and the upper dacitic melt pocket. (2) Underplating of primitive magma at the bottom of the chamber (Morgado *et al.*, 2019*a*, 2019*b*) may unlock the crystal mush via heat conduction and possibly fluid advection (Bachmann & Bergantz, 2003; Pistone *et al.*, 2017; Spera & Bohrson, 2018). These two mechanisms are not mutually exclusive, as the degassing of an underplating magma may also contribute to overpressurization in the magma chamber. Spera & Bohrson (2018) showed that 0·3 km^3 of crystal mush (i.e. the volume of magma erupted at Calbuco in 2015) might become unlocked in only a few weeks in highly viscous rhyolitic systems, and even shorter disaggregation timescales are expected for the andesitic crystal mush at Calbuco. Morgado *et al.* (2019*a*) attributed the unlocking of the crystal mush to magma underplating based on ilmenite–magnetite diffusion chronometry, and this is consistent with minor reverse zonings observed in some orthopyroxene crystals. However, they suggested that magma replenishment occurred within 4 days before the 2015 eruption, which seems too short a period given the size of the plagioclase rims. Arzilli *et al.* (2019) rejected the hypothesis of magma underplating based on the absence of minor-element compositional contrasts between plagioclase cores and rims and the absence of mafic enclaves in the eruptive products. We, however, emphasize that neither magma mixing nor small, centimeter- to decimeter-scale magma mingling is required to unlock the crystal mush (Pistone *et al.*, 2017; Spera & Bohrson, 2018; Morgado *et al.*, 2019*a*). Furthermore, we observed that plagioclase rims and cores do not have identical trace element concentrations, including those elements for which partitioning is not sensitive to plagioclase major element composition (i.e. REE). This indicates that plagioclase cores and rims crystallized from different melts, most probably owing to fractional crystallization, but perhaps also in part owing to magma mixing.

The most obvious products of differentiation in the shallow magma chamber are the relatively An-poor plagioclase rims and the small, unzoned plagioclase crystals (small crystal population in the CSDs; Fig. 5). Such Na-enriched rims form for two reasons: (1) after differentiation, the magma has evolved to a dacitic composition with a much lower CaO/Na_2O ratio than that of its parental basaltic andesite; (2) H_2O solubility

may be as low as 0·5 wt% in the shallow magma chamber (Moore & Carmichael, 1998), which drastically changes the composition of equilibrium plagioclase towards more albitic compositions compared with deeper, H_2O-rich magmas. Indeed, Pardini *et al.* (2018) showed that the glassy matrix of 2015 Calbuco eruptive products is depleted in volatiles. Finally, we agree with Arzilli *et al.* (2019) that over-pressurization of the magma chamber owing to fluid exsolution led to the failure of the thin (a few hundred meters thick) layer of overlying country rocks a few hours before the eruption, leading to the first phase of the sub-Plinian eruption with little warning.

CONCLUSIONS

After a 54 year non-eruptive period, Calbuco produced a sub-Plinian eruption in April 2015. The bulk composition of the eruptive products is dominantly basaltic andesite, comprising plagioclase, clinopyroxene, orthopyroxene, and minor magnetite in a dacitic melt. Plagioclase crystals are very strongly zoned with highly anorthitic cores and much more albitic rims, but lack any intermediate compositions between them. Based on petrography and detailed geochemistry, we propose the following sequence of events before the 2015 Calbuco eruption.

(1) A H_2O-rich basaltic andesite melt was emplaced at ~200–300 MPa and crystallized An-rich plagioclase and olivine, followed by clinopyroxene, orthopyroxene, and finally amphibole. After ~50–60 % crystallization, the residual melt became dacitic. Owing to significant heat loss to the magma chamber edges, the solidification process was dominated by *in situ* crystallization and crystal accumulation in an increasingly thick crystal mush.

(2) A few weeks to months before the 2015 eruption, the top, possibly poorly consolidated part of the crystal mush (crystals + evolved dacitic melt) was reactivated, perhaps by over-pressurization in the magma chamber following fluid exsolution and/or mafic underplating beneath the magma chamber (which may have also been degassing and contributing to over-pressurization of the crystal mush). The unlocked crystal-rich magma was then transported upwards to a very shallow storage region where H_2O solubility in the melt is low, and the dacitic melt crystallized more albitic plagioclase rims and a smaller population of unzoned plagioclase crystals. Our estimate of the mush reactivation timescale prior to eruption is based on the size of plagioclase rims and comparison with experiments (Larsen, 2005), and might include significant errors.

(3) As previously suggested (Arzilli *et al.*, 2019) and proposed for other andesitic volcanoes (Cassidy *et al.*, 2019), we propose that fluid saturation in the shallow magma chamber led to the rupture of overlying country rock. This may have occurred only a few days to hours before the eruption and allowed efficient transport of the crystal-rich andesitic magma to the surface.

Our study illustrates that caution should be exercised when interpreting the bulk-rock compositions of crystal-rich magmas. We have shown that the andesitic bulk-rock composition of the 2015 Calbuco eruptive products resulted from the accumulation of mush crystals in a pocket of dacitic melt. We hypothesize that such a process may occur at many intermediate arc volcanoes.

ACKNOWLEDGEMENTS

R. Almeev and I. Horn are thanked for their help with analyses. P. Samaniego is thanked for providing some samples used in this study. Discussions with D. Neave and F. Holtz were highly appreciated. Detailed comments from Dawn Ruth, Felipe Aguilera, an anonymous reviewer, and the editor Adam Kent were greatly appreciated and improved the paper. Robert Dennen is thanked for his help with editing the paper.

FUNDING

O.N. was supported by a postdoctoral mandate from the Fonds de la recherche scientifique (FNRS, Belgium; grant FC74042) and an Emmy Noether grant from the Deutsche Forschungsgemeinschaft (DFG, Germany).

APPENDIX A: ANALYTICAL METHODS

PETROGRAPHIC METHODS

Point counting

For all samples, a mechanical slide holder was repeatedly moved by 0·3 mm in both the *x* and *y* directions, generating 600–1500 points per slide. Olivine, clinopyroxene, orthopyroxene, Fe–Ti oxides, plagioclase, groundmass, and vesicles were counted as separate phases. Vesicle-free macrocryst mass fractions were calculated from the point counting data using the following phase densities: 3300 kg m^{-3} for olivine, 3200 kg m^{-3} for pyroxenes, and 2700 kg m^{-3} for plagioclase and groundmass.

Crystal size distribution

Plagioclase macrocryst CSDs were calculated for five selected samples. Following Ruth *et al.* (2016), crystal size data were obtained from high-quality BSE images (50–100× magnification). Using ImageJ software, we determined the total slide area, volumetric phase abundance, and vesicularity. We fitted an ellipse to each crystal (>5000) and used the long and short axes of each ellipse to calculate the CSDs. We did not apply stereological conversion. CSDs were evaluated following Neave *et al.* (2017*a*) on semi-logarithmic plots of number area density (N_A) normalized by bin width (bw) [i.e. ln(N_A/bw), mm^{-3}] vs the square root of crystal (ellipse) area ($A^{0.5}$). We note that some results become incoherent at $A^{0.5} < 200\,\mu$m owing to inefficient crystal separation. For two samples, we also performed plagioclase CSD analyses by tracing crystals on high-resolution thin-section scans (>1000 crystals for each

section). We obtained CSDs of similar shape to those obtained from the BSE images, although the absolute values (i.e. crystal population for each crystal size) were different. For these two samples, we also tested the effect of stereological conversion using CSDcorrections (Higgins, 2000) and best-fitting crystal shapes estimated using CSDslice (Morgan & Jerram, 2006). This again does not change the shape of the CSDs. We therefore present only CSD results obtained from BSE images, as that is our most comprehensive dataset.

X-RAY FLUORESCENCE

Five hundred grams of lapilli and pyroclast samples were washed in distilled water and dried prior to crushing. Bomb samples were first cut into blocks of 10–15 cm^3 before washing. All samples were dried, manually crushed with a hammer, and powdered in an agate ball-mill mortar. Loss on ignition was determined on 1 g of sample heated at 1000 °C. Major element analyses were performed on lithium tetra- and meta-borate fused glass discs prepared with 0·35 g of rock powder. Raw data were corrected following the Traill–Lachance algorithm and calibrated using 66 international standards (basalts, syenites, granites, ultramafic rocks, minerals, and soils). Trace elements (Co, Cu, Ni, Rb, Sr, Y, Zn, Zr, Ba, Cr, and V) were measured on pressed powder pellets. Except for Cr and V, data were corrected for matrix effects by Compton peak monitoring.

Repeated analyses ($n = 42$) of two international standards (BE-N and SBO-1; Govindaraju, 1994) were performed to test the accuracy of the ARL PERFORM-X 4200. The accuracy for all major elements is estimated to be better than ±2 % relative, except Na_2O (±8·1 %) and MnO (±4·4 %). Analytical precision (1σ) was estimated by repeated analyses of nine in-house standards (42 measurements of each standard) and is estimated to be better than ±5 % for major elements except Na_2O (±6·6 %). We calculated signal-to-noise ratios, which allow the true geological variability of our dataset to be distinguished from the variability owing to analytical uncertainty (MacLennan *et al.*, 2003; Neave, 2020). The variability of our Calbuco samples is considered statistically significant at the 95 % confidence level for all major elements except TiO_2, MnO, and P_2O_5, which are significant at the 75 % confidence level. For minor and trace elements, accuracy and precision were estimated by repeated analyses of three international standards (BHVO-1, STM-1, and SY-2; 10 measurements of each standard; Govindaraju, 1994). Accuracy is better than ±10 % for all trace elements except Cu (±26 %). Analytical precision (1σ) is better than ±3 % for all trace elements except Co (±6 %).

INDUCTIVELY COUPLED PLASMA MASS SPECTROMETRY

Prior to ICP-MS analyses, rock powders were dried overnight at 105 °C. Two hundred milligrams of powder were melted at 1000 °C for 60 min in 1 g of $LiBO_2$ (alkali fusion) in a Pt crucible. Molten samples were then dissolved in 5 % HNO_3 and diluted to a volume of 250 ml with distilled water. Samples were further diluted as necessary to decrease the total dissolved solids below 0·2 %. ICP-MS analyses were performed on a ThermoFisher Scientific X-Series 2 with a third-generation collision cell. The international standards BHVO-1, SGR-1, JB-3, and GA (Govindaraju, 1994) and multi-element in-house solutions of 5 and 10 ppb were used for calibration. Five other international standards (JGb-1, BHVO-2, BCR-2, JA-1, and CLS-1; Govindaraju, 1994) were measured to estimate accuracy, which was generally better than 10 % except for Zn (15 %), Cs (18 %), and Ta (12 %). Analytical precision was estimated by preparing six aliquots each of samples CL127 and CL153 and analysing them alongside the other samples. The 1σ relative errors are below 10 % for most elements except Cr, Ni, and Cu (1σ: 13–35 %). Sample variation is considered statistically significant at the 95 % confidence level for all elements except Cu, Zn, Ga, and Ge (70 % confidence level).

ELECTRON PROBE MICROANALYSIS

For both mineral and glass analyses, the following standards were used for Kα X-ray line calibration of the Cameca SX 100: albite (Al, Na), orthoclase (K), wollastonite (Si, Ca), TiO_2 (Ti), Fe_2O_3 (Fe), MgO (Mg), and Mn_3O_4 (Mn) following the procedure of Neave (2020). To ensure internal consistency across multiple analytical sessions, EPMA results were normalized to international standards. For glass analyses, we used VG-2 basalt glass (NMNH 111240-52). For minerals, we used Kakanui augite (NMNH 122142, using preferred values) for clinopyroxene, orthopyroxene, and plagioclase analyses and San Carlos olivine (NMNH 111312-44) for olivine analyses. Accuracy and precision were estimated by measuring the following standards during each session: A-99 (NMNH 113498) and BCR-2G (USGS) basaltic glasses and Lake County plagioclase (NMNH 115900) (Jarosewich *et al.*, 1980; Jochum *et al.*, 2005*b*). We also repeatedly measured in-house and Smithsonian microbeam standards of hypersthene, diopside, plagioclase [An_{95}; $An = 100 \times Ca/(Ca + Na)$, mol%] and olivine ($Fo_{83}$ and Fo_{10}). Major (>1 wt%) and minor (<1 wt%) element contents were determined with respective accuracies better than 2 % and 10 % and 1σ precisions better than 2 % and 15 %.

LASER ABLATION INDUCTIVELY COUPLED PLASMA MASS SPECTROMETRY

For LA-ICP-MS analyses, we used a ThermoScientific ElementXR fast-scanning sector-field ICP-MS system coupled to a laser ablation system based on a Spectra Physics Solstice 194 nm femtosecond laser. Samples were ablated by rastering a 30 μm laser spot over areas of $100 \times 100\ \mu m^2$ with a laser repetition rate of 20 Hz in a

He–Ar atmosphere. Five mass lines were measured for 5 ms each in the peak centres of each isotope, resulting in a total sweep time of ~1 s. Oxide formation rates were monitored by measuring ThO/Th ratios, which were always 0·1–0·4 %. Signals were acquired for a total of 120 s per analysis with the laser off for the first 40 s to determine background count rates. Samples were pre-rastered before analysis to remove surface contamination, and a 120 s gas evacuation time was used after pre-rastering to allow element signals to return to baseline levels. SiO_2 contents determined by EPMA were used as an internal standard (^{29}Si), and the BIR-1G glass standard was used for quantification (Jochum *et al.*, 2005*a*). Measurements of the BCR-2G glass standard indicate that most elemental analyses were accurate to better than 10 % relative, with only P, Cr, and Cu returning deviations >10 % relative.

MELT INCLUSION HOMOGENIZATION AND ANALYSIS

Olivine-hosted melt inclusions were heated at 1 atm using a rapid-quench Vernadsky-type heating stage mounted on a Nikon Eclipse LV100 petrographic microscope. Temperature was measured with an internal accuracy of 0·1 °C using an S-type ($Pt–Pt_{90}Rh_{10}$) thermocouple calibrated against the melting points of gold and silver. Heating was performed at $fO_2 = 10^{-10}$–10^{-12} atm in a purified He atmosphere. Oxygen fugacity was monitored using a zirconia probe at 700 °C, calibrated with $Ar–H_2$. The optimal stepped heating rates determined for this study to ensure equilibration during heating of the inclusions were 0·58 °C s^{-1} for 35 min, 0·28 °C s^{-1} for 10 min, and 0·18 °C s^{-1} until the last 'daughter' mineral has melted. When all daughter minerals had disappeared, the temperature was maintained for 10 min before quenching. After the heating experiments, the compositions of the melt inclusions were measured by EPMA on polished crystals and numerically corrected for post-entrapment crystallization. For these calculations, we used EPMA data obtained for the quenched inclusions and the host crystals a few micrometers away from the inclusions. The amount of olivine crystallization was estimated by adding increments of 0·1 % olivine to the melt composition until we obtained a difference smaller than 0·005 between the melt–olivine Mg–Fe partition coefficient and that predicted at 200 MPa by the thermodynamic model of Toplis (2005). To estimate the maximum errors on our results, we repeated this approach in a Monte Carlo simulation in which we allowed fO_2, which controls the melt $Fe^{3+}/\Sigma Fe$ ratio, to vary randomly between FMQ − 1 and FMQ + 1 (expressed in log units relative to the fayalite–magnetite–quartz oxygen buffer), and accounting for expected analytical errors on glass and olivine. The temperature effect on $Fe^{3+}/\Sigma Fe$ as a function of fO_2 was estimated using equations from Kress & Carmichael (1991) and Putirka (2008).

APPENDIX B: GEOROC COMPILATION

We used Georoc to compile bulk-rock data for all arcs worldwide (see the complete list in Supplementary Data Fig. 3), the Andean arc, and the SVZ. To retain only high-quality analyses, we selected only analyses in which every major element was measured and that returned totals between 98·5 and 101 wt%. We also calculated histograms for each major element and removed outliers (beyond 2σ from the mean). After filtering, our database contains >61 000 individual bulk-rock analyses, including 18 000 for the Andean arc and 4350 for the SVZ. Following Keller *et al.* (2015) and Pitcher & Kent (2019), we investigated the distribution of bulk-rock data using a bootstrap Monte Carlo analysis with sample weights inversely proportional to spatial sample density as obtained from GPS coordinates. We used the Matlab code of Keller *et al.* (2015), in which sample weighting coefficients (k) are calculated based on the density distribution of points on a sphere. Weighted sample density was calculated into bins of 1° latitude. We considered SiO_2 as the differentiation index and calculated the median and MAD in 2 wt% SiO_2 bins over 40–80 wt% SiO_2.

We also used Georoc to produce a filtered database of mineral compositions in magmas from arcs worldwide (orthopyroxene, $n = 9067$; clinopyroxene, $n = 8552$; plagioclase, $n = 19\,891$), the Andean arc (orthopyroxene, $n = 435$; clinopyroxene, $n = 1089$; plagioclase, $n = 2234$), and the SVZ (orthopyroxene, $n = 81$; clinopyroxene, $n = 221$; plagioclase, $n = 580$).

APPENDIX C: PYROXENE GEOTHERMOBAROMETER

TWO-PYROXENE GEOTHERMOBAROMETER (PUTIRKA, 2008)

In rocks from Calbuco, clinopyroxene and orthopyroxene crystals are rarely in direct contact, except in glomerocrysts. We therefore estimated temperature and pressure using all possible pairs of clinopyroxene and orthopyroxene analyses in individual samples, which yielded 45 767 pressure–temperature estimates. To estimate temperature, we used equations (36) and (37) of Putirka (2008), which have estimated maximum errors (standard error of estimate, SEE) of ~35 °C. To incorporate the error of the model into account, we converted the temperature estimates into kernel density estimates (KDEs) that were in turn fitted with a Gaussian function (Neave & Putirka, 2017). The KDEs were calculated with an imposed bandwidth of 35 °C, equivalent to the estimated SEE of the thermometer calibration. To evaluate how EPMA analytical errors might affect thethese temperature estimates, we ran a Monte Carlo simulation (50 simulations) for one sample, in which we considered that the errors on 4230 pyroxene couples are normally distributed around average values. Accounting for these errors has no effect on the average clinopyroxene–orthopyroxene equilibrium temperature, but

increases the standard deviation by 5% relative. However, the standard deviation remains below or within the range of the thermometric models (28–45 °C; Putirka, 2008). To evaluate pressure we fitted KDEs to our pressure estimates with a bandwidth of 280 MPa, corresponding to the SEE of the Putirka (2008) models. We kept only clinopyroxene–orthopyroxene pairs within 1σ of the clinopyroxene–orthopyroxene FeO–MgO partition coefficient reported by Putirka (2008); that is, $K_{cpx-opx}^{(Fe-Mg)} = 1{\cdot}09 \pm 0{\cdot}14$, which reduced the dataset to 3747 pressure estimates.

CLINOPYROXENE–LIQUID GEOTHERMOBAROMETER (NEAVE & PUTIRKA, 2017)

The model of Neave & Putirka (2017) is calibrated based on experiments at crustal pressures and applicable to mafic–intermediate magmas at oxygen fugacity (fO_2) conditions between FMQ − 1 and FMQ + 1 (expressed in log units relative to the fayalite–magnetite–quartz oxygen buffer). We conducted a first set of calculations based solely on the chemical compositions of our samples (bulk-rock and clinopyroxene) using an iterative melt-matching algorithm (Neave & Putirka, 2017). Putative equilibrium melts were sourced from individual glass matrix analyses and bulk-rock data, although we acknowledge that the glass matrix might be too evolved for use with this model (Neave & Putirka, 2017). Glass and clinopyroxene compositions were considered to be in equilibrium if the observed contents of the diopside–hedenbergite (Di–Hd), enstatite–ferrosilite (En–Fs), and Ca-Tschermakite (CaTs) components were within 1 SEE of predicted values [i.e. ±0·06 for Di–Hd, equation (7) from Mollo *et al.* (2013); ±0·05 for En–Fs, equation (6) from Mollo *et al.* (2013); ±0·03 for CaTs, equation (3.4) from Putirka (1999)]. We also used FeO–MgO partitioning between clinopyroxene and liquid, and considered them to be in equilibrium when the difference between the observed $K_{cpx-liq}^{(Fe-Mg)}$ value and that predicted using equation (35) of Putirka (2008) is <0·05. Based on the fO_2 of lavas from the nearby (8 km from Calbuco) and mineralogically similar La Picada volcano, we assumed an fO_2 value along the Ni–NiO (NNO) equilibrium (Vander Auwera *et al.*, 2019), which translates to a melt $Fe^{3+}/\Sigma Fe$ value of 0·20 as calculated using the model of Kress & Carmichael (1991). Morgado *et al.* (2019*a*) suggested a slightly more oxidized magma at Calbuco (NNO + 0·5), but this difference has almost no effect on the melt $Fe^{3+}/\Sigma Fe$ (0·21). This fO_2 estimate ($\log fO_2 = -8{\cdot}61$ at 1050 °C) is only slightly above the highest fO_2 conditions for which the use of the Neave & Putirka (2017) model is recommended (FMQ + 1; $\log fO_2 = -9{\cdot}36$ at 1050 °C). According to these equilibrium criteria and accounting for the oxidation state of the melt, none of the glass compositions can be considered to be in equilibrium with any of the clinopyroxene analyses owing to the low Mg# of the glass. Similarly, none of the bulk-rock compositions are in equilibrium with clinopyroxene. This confirms that the 2015 Calbuco eruptive products do not strictly represent liquid compositions, but rather the accumulation of crystals in a dacite melt.

To estimate the composition of the melts from which clinopyroxene may have crystallized at Calbuco, we performed a second set of iterative calculations in which the putative equilibrium liquid compositions were sourced from our Georoc compilation for the SVZ. Such an approach was previously used for several basaltic eruptions in Iceland (e.g. Winpenny & MacLennan, 2011; Neave & Putirka, 2017). We found 1020 clinopyroxene–liquid pairs potentially in equilibrium. Liquid compositions range from basaltic andesite to andesite (51–58 wt% SiO_2, 3–6 wt% MgO) and are not greatly different from Calbuco bulk-rock compositions. We applied the equations of Neave & Putirka (2017) to these liquid compositions and fitted KDEs with a bandwidth of 140 MPa (i.e. the estimated SEE of the barometer calibration) to account for the intrinsic model error. Temperature calculations must include an estimate of the melt H_2O content. Experimental results on basaltic andesite (Almeev *et al.*, 2013; Parat *et al.*, 2014) indicate that amphibole is stable in melts containing >4–6 wt% H_2O and appears after 30–50% crystallization of pyroxene + plagioclase ± olivine. As pyroxene appears on the liquidus much earlier than amphibole (Almeev *et al.*, 2013; Parat *et al.*, 2014; see also Fig. 14), we can safely consider that the melt from which pyroxene crystallized at Calbuco contained ~3–4 wt% H_2O. This value is in agreement with recent H_2O measurements in pyroxene-hosted melt inclusions from Calbuco (Arzilli *et al.*, 2019), although their values should be considered with great care as post-entrapment re-equilibration may occur within only a few hours (Portnyagin *et al.*, 2008; Gaetani *et al.*, 2012; Bucholz *et al.*, 2013; Loyd *et al.*, 2013; Neave *et al.*, 2017*b*).

APPENDIX D: REFORMULATION OF WATERS & LANGE (2015) MODEL

We reformulated the expression of Waters & Lange (2015) to output equilibrium plagioclase composition (An content) as a function of melt composition, including water and temperature. We note, however, that changing the temperature for a given melt composition significantly affects the calculated plagioclase composition. To circumvent this issue, we used our compiled experimental database to regress a thermometer that predicts the plagioclase liquidus as a function of melt composition, including water and pressure. We performed multiple linear regressions in a Monte Carlo simulation accounting for EPMA errors on the determination of melt composition ($\pm 1\sigma$) and likely errors on experimental temperature (up to 5 °C for experiments performed in 1 atm furnaces, cold-seal pressure vessels, and internally heated pressure vessels, and up to 20 °C for experiments performed in piston cylinders).

Our model predicts liquidus temperatures with a SEE of ±33 °C (Supplementary Data Fig. 8). We then used our reformulated expression of the Waters & Lange (2015) plagioclase–liquid hygrometer to calculate plagioclase compositions in equilibrium with 4350 bulk-rock compositions from the SVZ. We ran a Monte Carlo simulation in which we allowed the melt H_2O content to vary between 1 and 8 wt%, spanning the range reported by Arzilli *et al.* (2019). For each liquid composition and H_2O content, we calculated a liquidus temperature that we allowed to vary within the SEE of our empirical thermometer.

SUPPLEMENTARY DATA

Supplementary data are available at *Journal of Petrology* online.

REFERENCES

Almeev, R. R., Holtz, F., Ariskin, A. A. & Kimura, J. I. (2013). Storage conditions of Bezymianny volcano parental magmas: results of phase equilibria experiments at 100 and 700 MPa. *Contributions to Mineralogy and Petrology* **166**, 1389–1414.

Anderson, A. T. (1976). Magma mixing: petrological process and volcanological tool. *Journal of Volcanology and Geothermal Research* **1**, 3–33.

Annen, C., Blundy, J. D. & Sparks, R. S. J. (2006). The genesis of intermediate and silicic magmas in deep crustal hot zones. *Journal of Petrology* **47**, 505–539.

Annen, C., Blundy, J. D., Leuthold, J. & Sparks, R. S. J. (2015). Construction and evolution of igneous bodies: Towards an integrated perspective of crustal magmatism. *Lithos* **230**, 206–221.

Arzilli, F., Morgavi, D., Petrelli, M., Polacci, M., Burton, M., Di Genova, D., Spina, L., La Spina, G., Hartley, M. E., Romero, J. E., Fellowes, J., Diaz-Alvarado, J. & Perugini, D. (2019). The unexpected explosive sub-Plinian eruption of Calbuco volcano (22–23 April 2015; Southern Chile): triggering mechanism implications. *Journal of Volcanology and Geothermal Research* **378**, 35–50.

Assumpção, M., Feng, M., Tassara, A. & Julià, J. (2013). Models of crustal thickness for South America from seismic refraction, receiver functions and surface wave tomography. *Tectonophysics* **609**, 82–96.

Bachmann, O. & Bergantz, G. W. (2003). Rejuvenation of the Fish Canyon magma body: a window into the evolution of large-volume silicic magma systems. *Geology* **31**, 789–792.

Bachmann, O. & Bergantz, G. W. (2004). On the origin of crystal-poor rhyolites: extracted from batholitic crystal mushes. *Journal of Petrology* **45**, 1565–1582.

Bachmann, O., Miller, C. F. & de Silva, S. L. (2007). The volcanic–plutonic connection as a stage for understanding crustal magmatism. *Journal of Volcanology and Geothermal Research* **167**, 1–23.

Bacon, C. R. & Druitt, T. H. (1988). Compositional evolution of the zoned calcalkaline magma chamber of Mount Mazama, Crater Lake, Oregon. *Contributions to Mineralogy and Petrology* **98**, 224–256.

Baker, M. B., Grove, T. L. & Price, R. (1994). Primitive basalts and andesites from the Mt. Shasta region, N. California: products of varying melt fraction and water content. *Contributions to Mineralogy and Petrology* **118**, 111–129.

Bennett, E. N., Lissenberg, C. J. & Cashman, K. V. (2019). The significance of plagioclase textures in mid-ocean ridge basalt (Gakkel Ridge, Arctic Ocean). *Contributions to Mineralogy and Petrology* **174**, 49.

Blatter, D. L., Sisson, T. W. & Hankins, W. B. (2017). Voluminous arc dacites as amphibole reaction-boundary liquids. *Contributions to Mineralogy and Petrology* **172**, 27.

Blundy, J. D. & Holland, T. J. (1990). Calcic amphibole equilibria and a new amphibole–plagioclase geothermometer. *Contributions to Mineralogy and Petrology* **104**, 208–224.

Botcharnikov, R. E., Holtz, F., Almeev, R. R., Sato, H. & Behrens, H. (2008). Storage conditions and evolution of andesitic magma prior to the 1991–95 eruption of Unzen volcano: constraints from natural samples and phase equilibria experiments. *Journal of Volcanology and Geothermal Research* **175**, 168–180.

Browne, B. L., Eichelberger, J. C., Patino, L. C., Vogel, T. A., Uto, K. & Hoshizumi, H. (2006). Magma mingling as indicated by texture and Sr/Ba ratios of plagioclase phenocrysts from Unzen volcano, SW Japan. *Journal of Volcanology and Geothermal Research* **154**, 103–116.

Bucholz, C. E., Gaetani, G. A., Behn, M. D. & Shimizu, N. (2013). Post-entrapment modification of volatiles and oxygen fugacity in olivine-hosted melt inclusions. *Earth and Planetary Science Letters* **374**, 145–155.

Burgisser, A. & Bergantz, G. W. (2011). A rapid mechanism to remobilize and homogenize highly crystalline magma bodies. *Nature* **471**, 212–215.

Cashman, K. (1993). Relationship between plagioclase crystallization and cooling rate in basaltic melts. *Contributions to Mineralogy and Petrology* **113**, 126–142.

Cashman, K. & Blundy, J. (2013). Petrological cannibalism: the chemical and textural consequences of incremental magma body growth. *Contributions to Mineralogy and Petrology* **166**, 703–729.

Cashman, K. V. & Edmonds, M. (2019). Mafic glass compositions: a record of magma storage conditions, mixing and ascent. *Philosophical Transactions of the Royal Society A* **377**, 20180004.

Cashman, K. V., Sparks, R. S. J. & Blundy, J. D. (2017). Vertically extensive and unstable magmatic systems: a unified view of igneous processes. *Science* **355**, eaag3055.

Cassidy, M., Ebmeier, S. K., Helo, C., Watt, S. F. L., Caudron, C., Odell, A., Spaans, K., Kristianto, P., Triastuty, H., Gunawan, H. & Castro, J. M. (2019). Explosive eruptions with little warning: Experimental petrology and volcano monitoring observations from the 2014 eruption of Kelud, Indonesia. *Geochemistry, Geophysics, Geosystems* **20**, 4218–4247.

Castruccio, A. & Clavero, J. (2015). Lahar simulation at active volcanoes of the Southern Andes: implications for hazard assessment. *Natural Hazards* **77**, 693–716.

Castruccio, A., Clavero, J. & Rivera, A. (2010). Comparative study of lahars generated by the 1961 and 1971 eruptions of Calbuco and Villarrica volcanoes, Southern Andes of Chile. *Journal of Volcanology and Geothermal Research* **190**, 297–311.

Castruccio, A., Clavero, J., Segura, A., Samaniego, P., Roche, O., Le Pennec, J.-L. & Droguett, B. (2016). Eruptive parameters and dynamics of the April 2015 sub-Plinian eruptions of Calbuco volcano (southern Chile). *Bulletin of Volcanology* **78**, 62.

Conway, C. E., Chamberlain, K. J., Harigane, Y., Morgan, D. J. & Wilson, C. J. (2020). Rapid assembly of high-Mg andesites and dacites by magma mixing at a continental arc stratovolcano. *Geology*

Cooper, K. M. & Kent, A. J. (2014). Rapid remobilization of magmatic crystals kept in cold storage. *Nature* **506**, 480–483.

Cooper, K. M. & Reid, M. R. (2003). Re-examination of crystal ages in recent Mount St. Helens lavas: implications for magma reservoir processes. *Earth and Planetary Science Letters* **213**, 149–167.

Costa, F., Coogan, L. A. & Chakraborty, S. (2010). The time scales of magma mixing and mingling involving primitive melts and melt–mush interaction at mid-ocean ridges. *Contributions to Mineralogy and Petrology* **159**, 371–387.

Couch, S., Harford, C., Sparks, R. & Carroll, M. (2003). Experimental constraints on the conditions of formation of highly calcic plagioclase microlites at the Soufrière Hills Volcano, Montserrat. *Journal of Petrology* **44**, 1455–1475.

Davidson, J., Turner, S. & Plank, T. (2013). Dy/Dy: Variations arising from mantle sources and petrogenetic processes. *Journal of Petrology* **54**, 525–537.

Delgado, F., Pritchard, M. E., Ebmeier, S., González, P. & Lara, L. (2017). Recent unrest (2002–2015) imaged by space geodesy at the highest risk Chilean volcanoes: Villarrica, Llaima, and Calbuco (Southern Andes). *Journal of Volcanology and Geothermal Research* **344**, 270–288.

Drignon, M. J., Nielsen, R. L., Tepley, F. J., III & Bodnar, R. J. (2018). Upper mantle origin of plagioclase megacrysts from plagioclase-ultraphyric mid-oceanic ridge basalt. *Geology* **47**, 43–46.

Druitt, T. H., Costa, F., Deloule, E., Dungan, M. & Scaillet, B. (2012). Decadal to monthly timescales of magma transfer and reservoir growth at a caldera volcano. *Nature* **482**, 77–80.

Dzierma, Y., Thorwart, M., Rabbel, W., Siegmund, C., Comte, D., Bataille, K., Iglesia, P. & Prezzi, C. (2012). Moho topography and subducting oceanic slab of the Chilean continental margin in the maximum slip segment of the 1960 Mw 9.5 Valdivia (Chile) earthquake from P-receiver functions. *Tectonophysics* **530–531**, 180–192.

Eichelberger, J. C. (1978). Andesitic volcanism and crustal evolution. *Nature* **275**, 21–27.

Eichelberger, J. C., Izbekov, P. E. & Browne, B. L. (2006). Bulk chemical trends at arc volcanoes are not liquid lines of descent. *Lithos* **87**, 135–154.

Ellis, B. S., Bachmann, O. & Wolff, J. A. (2014). Cumulate fragments in silicic ignimbrites: the case of the Snake River Plain. *Geology* **42**, 431–434.

Erdmann, S., Martel, C., Pichavant, M. & Kushnir, A. (2014). Amphibole as an archivist of magmatic crystallization conditions: problems, potential, and implications for inferring magma storage prior to the paroxysmal 2010 eruption of Mount Merapi, Indonesia. *Contributions to Mineralogy and Petrology* **167**, 1016.

Gaetani, G. A., O'Leary, J. A., Shimizu, N., Bucholz, C. E. & Newville, M. (2012). Rapid reequilibration of H_2O and oxygen fugacity in olivine-hosted melt inclusions. *Geology* **40**, 915–918.

Ganne, J., Bachmann, O. & Feng, X. (2018). Deep into magma plumbing systems: interrogating the crystal cargo of volcanic deposits. *Geology* **46**, 415–418.

Ghiorso, M. S. (1997). Thermodynamic models of igneous processes. *Annual Review of Earth and Planetary Sciences* **25**, 221–241.

Ghiorso, M. S. & Sack, R. O. (1995). Chemical mass transfer in magmatic processes IV. A revised and internally consistent thermodynamic model for the interpolation and extrapolation of liquid–solid equilibria in magmatic systems at elevated temperatures and pressures. *Contributions to Mineralogy and Petrology* **119**, 197–212.

Gorini, A., Ridolfi, F., Piscaglia, F., Taussi, M. & Renzulli, A. (2018). Application and reliability of calcic amphibole thermobarometry as inferred from calc-alkaline products of active geothermal areas in the Andes. *Journal of Volcanology and Geothermal Research* **358**, 58–76.

Govindaraju, K. (1994). Compilation of working values and sample preparation for 383 geostandards. *Geostandards and Geoanalytical Research* **18**, 1–158.

Grove, T. L. & Kinzler, R. J. (1986). Petrogenesis of andesites. *Annual Review of Earth and Planetary Sciences* **14**, 417–454.

Grove, T. L., Parman, S. W., Bowring, S. A., Price, R. C. & Baker, M. B. (2002). The role of an H_2O-rich fluid component in the generation of primitive basaltic andesites and andesites from the Mt. Shasta region, N California. *Contributions to Mineralogy and Petrology* **142**, 375–396.

Grove, T. L., Elkins-Tanton, L. T., Parman, S. W., Chatterjee, N., Müntener, O. & Gaetani, G. A. (2003). Fractional crystallization and mantle-melting controls on calc-alkaline differentiation trends. *Contributions to Mineralogy and Petrology* **145**, 515–533.

Gualda, G. A., Ghiorso, M. S., Lemons, R. V. & Carley, T. L. (2012). Rhyolite-melts: a modified calibration of melts optimized for silica-rich, fluid-bearing magmatic systems. *Journal of Petrology* **53**, 875–890.

Hamada, M., Kawamoto, T., Takahashi, E. & Fujii, T. (2011). Polybaric degassing of island arc low-K tholeiitic basalt magma recorded by OH concentrations in Ca-rich plagioclase. *Earth and Planetary Science Letters* **308**, 259–266.

Hickey-Vargas, R., Sun, M. & Holbik, S. (2016). Geochemistry of basalts from small eruptive centers near Villarrica stratovolcano, Chile: evidence for lithospheric mantle components in continental arc magmas. *Geochimica et Cosmochimica Acta* **185**, 358–382.

Higgins, M. D. (2000). Measurement of crystal size distributions. *American Mineralogist* **85**, 1105–1116.

Higgins, M. D. & Roberge, J. (2007). Three magmatic components in the 1973 eruption of Eldfell volcano, Iceland: evidence from plagioclase crystal size distribution (CSD) and geochemistry. *Journal of Volcanology and Geothermal Research* **161**, 247–260.

Higgins, M. D., Voos, S. & Vander Auwera, J. (2015). Magmatic processes under Quizapu volcano, Chile, identified from geochemical and textural studies. *Contributions to Mineralogy and Petrology* **170**, 51.

Hildreth, W. & Moorbath, S. (1988). Crustal contributions to arc magmatism in the Andes of central Chile. *Contributions to Mineralogy and Petrology* **98**, 455–489.

Holtz, F., Sato, H., Lewis, J., Behrens, H. & Nakada, S. (2004). Experimental petrology of the 1991–1995 Unzen dacite, Japan. Part I: phase relations, phase composition and pre-eruptive conditions. *Journal of Petrology* **46**, 319–337.

Huber, C., Bachmann, O. & Manga, M. (2010). Two competing effects of volatiles on heat transfer in crystal-rich magma: thermal insulation vs defrosting. *Journal of Petrology* **51**, 847–867.

Huber, C., Bachmann, O. & Dufek, J. (2011). Thermo-mechanical reactivation of locked crystal mushes: melting-induced internal fracturing and assimilation processes in magmas. *Earth and Planetary Science Letters* **304**, 443–454.

Humphreys, M. C. S., Blundy, J. D. & Sparks, R. S. J. (2006). Magma evolution and open-system processes at Shiveluch volcano: insights from phenocryst zoning. *Journal of Petrology* **47**, 2303–2334.

Humphreys, M. C. S., Christopher, T. & Hards, V. (2009). Microlite transfer by disaggregation of mafic inclusions following magma mixing at Soufrière Hills volcano, Montserrat. *Contributions to Mineralogy and Petrology* **157**, 609–624.

Izbekov, P. E., Eichelberger, J. C., Patino, L. C., Vogel, T. A. & Ivanov, B. V. (2002). Calcic cores of plagioclase phenocrysts

in andesite from Karymsky volcano: evidence for rapid introduction by basaltic replenishment. *Geology* **30**, 799–802.

Jarosewich, E., Nelen, J. & Norberg, J. A. (1980). Reference samples for electron microprobe analysis. *Geostandards and Geoanalytical Research* **4**, 43–47.

Jennings, E. S. & Holland, T. J. B. (2015). A simple thermodynamic model for melting of peridotite in the system NCFMASOCr. *Journal of Petrology* **56**, 869–892.

Jochum, K. P., Pfander, J., Woodhead, J. D., Willbold, M., Stoll, B., Herwig, K., Amini, M., Abouchami, W. & Hofmann, A. W. (2005a). MPI-DING glasses: new geological reference materials for *in situ* Pb isotope analysis. *Geochemistry, Geophysics, Geosystems* **6, Q10008**.

Jochum, K. P., Willbold, M., Raczek, I., Stoll, B. & Herwig, K. (2005b). Chemical characterisation of the USGS reference glasses GSA-1G, GSC-1G, GSD-1G, GSE-1G, BCR-2G, BHVO-2G and BIR-1G using EPMA, ID-TIMS, ID-ICP-MS and LA-ICP-MS. *Geostandards and Geoanalytical Research* **29**, 285–302.

Kahl, M., Chakraborty, S., Pompilio, M. & Costa, F. (2015). Constraints on the nature and evolution of the magma plumbing system of Mt. Etna Volcano (1991–2008) from a combined thermodynamic and kinetic modelling of the compositional record of minerals. *Journal of Petrology* **56**, 2025–2068.

Keller, C. B., Schoene, B., Barboni, M., Samperton, K. M. & Husson, J. M. (2015). Volcanic–plutonic parity and the differentiation of the continental crust. *Nature* **523**, 301–307.

Kemner, F., Haase, K. M., Beier, C., Krumm, S. & Brandl, P. A. (2015). Formation of andesite melts and Ca-rich plagioclase in the submarine Monowai volcanic system, Kermadec arc. *Geochemistry, Geophysics, Geosystems* **16**, 4130–4152.

Kent, A. J. R. (2008). Melt inclusions in basaltic and related volcanic rocks. In: Putirka, K. D. & Tepley III, F. J. T. (eds) Minerals, Inclusions and Volcanic Processes. *Mineralogical Society of America and Geochemical Society, Reviews in Mineralogy and Geochemistry* **69**, 273–331.

Kent, A. J. R., Darr, C., Koleszar, A. M., Salisbury, M. J. & Cooper, K. M. (2010). Preferential eruption of andesitic magmas through recharge filtering. *Nature Geoscience* **3**, 631–636.

Kohut, E. J. & Nielsen, R. L. (2003). Low-pressure phase equilibria of anhydrous anorthite-bearing mafic magmas. *Geochemistry, Geophysics, Geosystems* **4, 1057**.

Kress, V. C. & Carmichael, I. S. E. (1991). The compressibility of silicate liquids containing Fe_2O_3 and the effect of composition, temperature, oxygen fugacity and pressure on their redox states. *Contributions to Mineralogy and Petrology* **108**, 82–92.

Langmuir, C. H. (1989). Geochemical consequences of *in situ* crystallization. *Nature* **340**, 199–205.

Larsen, J. F. (2005). Experimental study of plagioclase rim growth around anorthite seed crystals in rhyodacitic melt. *American Mineralogist* **90**, 417–427.

Leake, B. E., Woolley, A. R., Arps, C. E. S., Birch, W. D., Gilbert, M. C., Grice, J. D., Hawthorne, F. C., Kato, A., Kisch, H. J., Krivovichev, V. G., Linthout, K., Laird, J., Mandarino, J. A., Maresch, W. V., Nickel, E. H., Rock, N. M. S., Schumacher, J. C., Smith, D. C., Stephenson, N. C. N., Ungaretti, L., Whittaker, E. J. W. & Guo, Y. Z. (1997). Nomenclature of amphiboles: report of the subcommittee on amphiboles of the International Mineralogical Association, commission on new minerals and mineral names. *American Mineralogist* **82**, 1019–1037.

Lee, C. T. & Bachmann, O. (2014). How important is the role of crystal fractionation in making intermediate magmas? Insights from Zr and P systematics. *Earth and Planetary Science Letters* **393**, 266–274.

Longhi, J., Vander Auwera, J., Fram, M. & Monthieth, J. N. (1993). Pressure effects, kinetics and rheology of anorthositic and related magmas. *American Mineralogist* **78**, 1016–1030.

Lopez-Escobar, L., Parada, M. A., Hickey-Vargas, R., Frey, F. A., Kempton, P. D., & Moreno, H. (1995). Calbuco Volcano and minor eruptive centers distributed along the Liquiñe-Ofqui Fault Zone, Chile (41–42°S): contrasting origin of andesitic and basaltic magma in the Southern Volcanic Zone of the Andes. Contributions to Mineralogy and Petrology, **119**, 345–361.

Lopez-Escobar, L., Parada, M. A., Moreno, H., Frey, F. A. & Hickey-Vargas, R. L. (1992). A contribution to the petrogenesis of Osorno and Calbuco volcanoes, southern Andes (41°00′–41°30′S): comparative study. *Andean Geology* **19**, 211–226.

Loyd, A. S., Plank, T., Ruprecht, P., Hauri, E. H. & Rose, W. (2013). Volatile loss from melt inclusions in pyroclasts of differing sizes. *Contributions to Mineralogy and Petrology* **165**, 129–153.

MacLennan, J., McKenzie, D., Gronvold, K. & Slater, L. (2001). Crustal accretion under Northern Iceland. *Earth and Planetary Science Letters* **191**, 295–310.

MacLennan, J., McKenzie, D., Hilton, F., Gronvold, K. & Shimizu, N. (2003). Geochemical variability in a single flow from northern Iceland. *Journal of Geophysical Research* **108**, 1–21.

Marsh, B. D. (1998). On the interpretation of crystal size distributions in magmatic systems. *Journal of Petrology* **39**, 553–599.

Melekhova, E., Blundy, J., Robertson, R. & Humphreys, M. C. (2015). Experimental evidence for polybaric differentiation of primitive arc basalt beneath St. Vincent, Lesser Antilles. *Journal of Petrology* **56**, 161–192.

Melekhova, E., Blundy, J., Martin, R., Arculus, R. & Pichavant, M. (2017). Petrological and experimental evidence for differentiation of water-rich magmas beneath St. Kitts, Lesser Antilles. *Contributions to Mineralogy and Petrology* **172**, 98.

Mollo, S., Putirka, K., Misiti, V., Soligo, M. & Scarlato, P. (2013). A new test for equilibrium based on clinopyroxene–melt pairs: clues on the solidification temperatures of Etnean alkaline melts at post-eruptive conditions. *Chemical Geology* **352**, 92–100.

Moore, G. & Carmichael, I. (1998). The hydrous phase equilibria (to 3 kbar) of an andesite and basaltic andesite from western Mexico: constraints on water content and conditions of phenocryst growth. *Contributions to Mineralogy and Petrology* **130**, 304–319.

Moreno, H. & Naranjo, J. A. (2004). Calbuco volcano historic block-and-ash and pyroclastic flows: increasing threatening on surrounding communities, Southern Andes 41.5°S. *IAVCEI General Assembly, Pucón, Chile, November 2004.*

Morgado, E., Morgan, D. J., Harvey, J., Parada, M.-Á., Castruccio, A., Brahm, R., Gutiérrez, F., Georgiev, B. & Hammond, S. J. (2019a). Localised heating and intensive magmatic conditions prior to the 22–23 April 2015 Calbuco volcano eruption (Southern Chile). *Bulletin of Volcanology* **81**, 24.

Morgado, E., Morgan, D., Castruccio, A., Ebmeier, S., Parada, M., Brahm, R., Harvey, J., Gutierrez, F. & Walshaw, R. (2019b). Old magma and a new, intrusive trigger: using diffusion chronometry to understand the rapid-onset Calbuco eruption, April 2015 (Southern Chile). *Contributions to Mineralogy and Petrology* **174**, 61

Morgan, D. J. & Jerram, D. A. (2006). On estimating crystal shape for crystal size distribution analysis. *Journal of Volcanology and Geothermal Research* **154**, 1–7.

Murphy, M. D., Sparks, R. S. J., Barclay, J., Carroll, M. R., Lejeune, A.-M., Brewer, T. S., Macdonald, R., Black, S. & Young, S. (1998). The role of magma mixing in triggering the current eruption at the Soufriere Hills volcano, Montserrat, West Indies. *Geophysical Research Letters* **25**, 3433–3436.

Mutch, E., Blundy, J., Tattitch, B., Cooper, F. & Brooker, R. (2016). An experimental study of amphibole stability in low-pressure granitic magmas and a revised Al-in-hornblende geobarometer. *Contributions to Mineralogy and Petrology* **171**, 85.

Nakamura, M. (1995). Continuous mixing of crystal mush and replenished magma in the ongoing Unzen eruption. *Geology* **23**, 807–810.

Nakamura, M. & Shimakita, S. (1998). Dissolution origin and syn-entrapment compositional change of melt inclusion in plagioclase. *Earth and Planetary Science Letters* **161**, 119–133.

Namur, O. & Charlier, B. (2017). Silicate mineralogy at the surface of Mercury. *Nature Geoscience* **10**, 9–13.

Namur, O. & Humphreys, M. C. (2018). Trace element constraints on the differentiation and crystal mush solidification in the Skaergaard intrusion, Greenland. *Journal of Petrology* **59**, 387–418.

Namur, O., Humphreys, M. C. S. & Holness, M. B. (2014). Crystallization of interstitial liquid and latent heat buffering in solidifying gabbros: Skaergaard intrusion, Greenland. *Journal of Petrology* **55**, 1389–1427.

Namur, O., Collinet, M., Charlier, B., Grove, T. L., Holtz, F. & McCammon, C. (2016). Melting processes and mantle sources of lavas on Mercury. *Earth and Planetary Science Letters* **439**, 117–128.

Neave, D. A. (2020). Chemical variability in peralkaline magmas and magma reservoirs: insights from the Khaggiar lava flow, Pantelleria, Italy. *Contributions to Mineralogy and Petrology* **175**, 39.

Neave, D. A. & Putirka, K. D. (2017). A new clinopyroxene–liquid barometer, and implications for magma storage pressures under Icelandic rift zones. *American Mineralogist* **102**, 777–794.

Neave, D. A., Maclennan, J., Hartley, M. E., Edmonds, M. & Thordarson, T. (2014). Crystal storage and transfer in basaltic systems: the Skuggafjoll eruption, Iceland. *Journal of Petrology* **55**, 2311–2346.

Neave, D. A., Buisman, I. & Maclennan, J. (2017a). Continuous mush disaggregation during the long-lasting Laki fissure eruption, Iceland. *American Mineralogist* **102**, 2007–2021.

Neave, D. A., Hartley, M. E., Maclennan, J., Edmonds, M. & Thordarson, T. (2017b). Volatile and light lithophile elements in high-anorthite plagioclase-hosted melt inclusions from Iceland. *Geochimica et Cosmochimica Acta* **205**, 100–118.

Neave, D. A., Shorttle, O., Oeser, M., Weyer, S. & Kobayashi, K. (2018). Mantle-derived trace element variability in olivines and their melt inclusions. *Earth and Planetary Science Letters* **483**, 90–104.

Nelson, S. T. & Montana, A. (1992). Sieve-textured plagioclase in volcanic rocks produced by rapid decompression. *American Mineralogist* **77**, 1242–1249.

O'Neill, H. S. C. (2016). The smoothness and shapes of chondrite-normalized rare earth element patterns in basalts. *Journal of Petrology* **57**, 1463–1508.

Panjasawatwong, Y., Danyushevsky, L. V., Crawford, A. J. & Harris, K. L. (1995). An experimental study of the effects of melt composition on plagioclase–melt equilibria at 5 and 10 kbar: implications for the origin of magmatic high-An plagioclase. *Contributions to Mineralogy and Petrology* **118**, 420–432.

Parat, F., Streck, M., Holtz, F. & Almeev, R. (2014). Experimental study into the petrogenesis of crystal-rich basaltic to andesitic magmas at Arenal volcano. *Contributions to Mineralogy and Petrology* **168**, 1040.

Pardini, F., Burton, M., Arzilli, F., La Spina, G. & Polacci, M. (2018). SO_2 emissions, plume heights and magmatic processes inferred from satellite data: The 2015 Calbuco eruptions. *Journal of Volcanology and Geothermal Research* **361**, 12–24.

Passmore, E., MacLennan, J., Fitton, G. & Thordarson, T. (2012). Mush disaggregation in basaltic magma chambers: Evidence from the AD 1783 Laki eruption. *Journal of Petrology* **53**, 2593–2623.

Pistone, M., Blundy, J. & Brooker, R. A. (2017). Water transfer during magma mixing events: Insights into crystal mush rejuvenation and melt extraction processes. *American Mineralogist* **102**, 766–776.

Pitcher, B. W. & Kent, A. J. (2019). Statistics and segmentation: using Big Data to assess Cascades Arc compositional variability. *Geochimica et Cosmochimica Acta* **265**, 443–467.

Portnyagin, M., Almeev, R., Matveev, S. & Holtz, F. (2008). Experimental evidence for rapid water exchange between melt inclusions in olivine and host magma. *Earth and Planetary Science Letters* **272**, 541–552.

Pupier, E., Duchene, S. & Toplis, M. J. (2008). Experimental quantification of plagioclase crystal size distribution during cooling of a basaltic liquid. *Contributions to Mineralogy and Petrology* **155**, 555–570.

Putirka, K. (1999). Clinopyroxene + liquid equilibria to 100 kbar and 2450 K. *Contributions to Mineralogy and Petrology* **135**, 151–163.

Putirka, K. (2016). Amphibole thermometers and barometers for igneous systems and some implications for eruption mechanisms of felsic magmas at arc volcanoes. *American Mineralogist* **101**, 841–858.

Putirka, K. D. (2008). Thermometers and barometers for volcanic systems. In: Putirka, K. D. & Tepley III, F. J. T. (eds) Minerals, Inclusions and Volcanic Processes. *Mineralogical Society of America and Geochemical Society, Reviews in Mineralogy and Geochemistry* **69**, 61–120.

Reubi, O. & Blundy, J. (2009). A dearth of intermediate melts at subduction zone volcanoes and the petrogenesis of arc andesites. *Nature* **461**, 1269–1273.

Ridolfi, F. & Renzulli, A. (2012). Calcic amphiboles in calc-alkaline and alkaline magmas: thermobarometric and chemometric empirical equations valid up to 1,130°C and 2·2 GPa. *Contributions to Mineralogy and Petrology* **163**, 877–895.

Ridolfi, F., Renzulli, A. & Puerini, M. (2010). Stability and chemical equilibrium of amphibole in calc-alkaline magmas: an overview, new thermobarometric formulations and application to subduction-related volcanoes. *Contributions to Mineralogy and Petrology* **160**, 45–66.

Romero, J. E., Morgavi, D., Arzilli, F., Daga, R., Caselli, A., Reckziegel, F., Viramonte, J., Díaz-Alvarado, J., Polacci, M., Burton, M. & Perugini, D. (2016). Eruption dynamics of the 22–23 April 2015 Calbuco volcano (Southern Chile): analyses of tephra fall deposits. *Journal of Volcanology and Geothermal Research* **317**, 15–29.

Rudnick, R. L. & Gao, S. (2003). Composition of the continental crust. In: Holland, H. D. & Turekian, K. K. (eds) The Crust. *Treatise on Geochemistry, Amsterdam* **3**, 1–64.

Ruprecht, P., Bergantz, G. W., Cooper, K. M. & Hildreth, W. (2012). The crustal magma storage system of Volcan Quizapu, Chile, and the effects of magma mixing on magma diversity. *Journal of Petrology* **53**, 801–840.

Ruth, D. C., Cottrell, E., Cortés, J. A., Kelley, K. A. & Calder, E. S. (2016). From passive degassing to violent strombolian eruption: the case of the 2008 eruption of Llaima volcano, Chile. *Journal of Petrology* **57**, 1833–1864.

Salisbury, M. J., Bohrson, W. A., Clynne, M. A., Ramos, F. C. & Hoskin, P. (2008). Multiple plagioclase crystal populations identified by crystal size distribution and *in situ* chemical data: implications for timescales of magma chamber processes associated with the 1915 eruption of Lassen Peak, CA. *Journal of Petrology* **49**, 1755–1780.

Scaillet, B. & Evans, B. (1999). The 15 June 1991 eruption of Mount Pinatubo. I. Phase equilibria and pre-eruption P–T–fO_2–fH_2O conditions of the dacite magma. *Journal of Petrology* **40**, 381–411.

Schiavi, F., Provost, A., Schiano, P. & Cluzel, N. (2016). P–V–T–X evolution of olivine-hosted melt inclusions during high-temperature homogenization treatment. *Geochimica et Cosmochimica Acta* **172**, 1–21.

Sellés, D. & Moreno, H. (2011). *Geología del Volcán Calbuco: región de Los Lagos*. Servicio Nacional de Geología y Minería, Santiago.

Sellés, D., Rodríguez, A., Dungan, M. A., Naranjo, J. A. & Gardeweg, M. (2004). Geochemistry of Nevado de Longaví Volcano (36·2°S): a compositionally a typical arc volcano in the Southern Volcanic Zone of the Andes. *Revista Geológica de Chile* **31**, 293–315.

Shea, T. & Hammer, J. E. (2013). Kinetics of cooling- and decompression-induced crystallization in hydrous mafic–intermediate magmas. *Journal of Volcanology and Geothermal Research* **260**, 127–145.

Sisson, T. W. & Grove, T. L. (1993). Experimental investigations of the role of H_2O in calc-alkaline differentiation and subduction zone magmatism. *Contributions to Mineralogy and Petrology* **113**, 143–166.

Sobolev, A. V. & Danyushevsky, L. V. (1994). Petrology and geochemistry of boninites from the north termination of the Tonga Trench: constraints on the generation conditions of primary high-Ca boninite magmas. *Journal of Petrology* **35**, 1183–1211.

Spera, F. J. & Bohrson, W. A. (2018). Rejuvenation of crustal magma mush: a tale of multiply nested processes and timescales. *American Journal of Science* **318**, 90–140.

Stechern, A., Just, T., Holtz, F., Blume-Oeste, M. & Namur, O. (2017). Decoding magma plumbing and geochemical evolution beneath the Lastarria volcanic complex (Northern Chile)? Evidence for multiple magma storage regions. *Journal of Volcanology and Geothermal Research* **338**, 25–45.

Stern, C. R. (2004). Active Andean volcanism: its geologic and tectonic setting. *Revista Geológica de Chile* **31**, 161–206.

Stock, M. J., Humphreys, M. C., Smith, V. C., Isaia, R. & Pyle, D. M. (2016). Late-stage volatile saturation as a potential trigger for explosive volcanic eruptions. *Nature Geoscience* **9**, 249–254.

Streck, M. J. (2008). Mineral textures and zoning as evidence for open system processes. In: Putirka, K. D. & Tepley III, F. J. T. (eds) Minerals, Inclusions and Volcanic Processes. *Mineralogical Society of America and Geochemical Society, Reviews in Mineralogy and Geochemistry* **69**, 595–622.

Syracuse, E. M., van Keken, P. E. & Abers, G. A. (2010). The global range of subduction zone thermal models. *Physics of the Earth and Planetary Interiors* **183**, 73–90.

Tasarova, Z. A. (2007). Towards understanding the lithospheric structure of the southern Chilean subduction zone (36°S–42°) and its role in the gravity field. *Geophysical Journal International* **170**, 995–1014.

Taylor, S. R. & McLennan, S. M. (1985). *The Continental Crust: its Composition and Evolution*. Oxford: Blackwell Scientific, 312 pp.

Toplis, M. J. (2005). The thermodynamics of iron and magnesium partitioning between olivine and liquid: criteria for assessing and predicting equilibrium in natural and experimental systems. *Contributions to Mineralogy and Petrology* **149**, 22–39.

Turner, S., George, R., Jerram, D. A., Carpenter, N. & Hawkesworth, C. (2003). Case studies of plagioclase growth and residence times in island arc lavas from Tonga and the Lesser Antilles, and a model to reconcile discordant age information. *Earth and Planetary Science Letters* **214**, 279–294.

Ulmer, P., Kaegi, R. & Müntener, O. (2018). Experimentally derived intermediate to silica-rich arc magmas by fractional and equilibrium crystallization at 1·0 GPa: an evaluation of phase relationships, compositions, liquid lines of descent and oxygen fugacity. *Journal of Petrology* **59**, 11–58.

Vander Auwera, J., Namur, O., Dutrieux, A., Wilkinson, C. M., Ganerød, M., Coumont, V. & Bolle, O. (2019). Mantle melting and magmatic processes under La Picada stratovolcano (CSVZ, Chile). *Journal of Petrology* **60**, 907–944.

Van Eaton, A. R., Amigo, Á., Bertin, D., Mastin, L. G., Giacosa, R. E., González, J., Valderrama, O., Fontijn, K. & Behnke, S. A. (2016). Volcanic lightning and plume behavior reveal evolving hazards during the April 2015 eruption of Calbuco volcano, Chile. *Geophysical Research Letters* **43**, 3563–3571.

Wanke, M., Clynne, M. A., von Quadt, A., Vennemann, T. W. & Bachmann, O. (2019). Geochemical and petrological diversity of mafic magmas from Mount St. Helens. *Contributions to Mineralogy and Petrology* **174**, 10.

Waters, L. E. & Lange, R. A. (2015). An updated calibration of the plagioclase–liquid hygrometer–thermometer applicable to basalts through rhyolites. *American Mineralogist* **100**, 2172–2184.

Watt, S. F. L., Pyle, D. M., Naranjo, J. A., Rosqvist, G., Mella, M., Mather, T. A. & Moreno, H. (2011). Holocene tephrochronology of the hualaihue region (Andean southern volcanic zone, ~42°S), Southern Chile. *Quaternary International* **246**, 324–343.

Watt, S. F., Pyle, D. M., Mather, T. A. & Naranjo, J. A. (2013). Arc magma compositions controlled by linked thermal and chemical gradients above the subducting slab. *Geophysical Research Letters* **40**, 2550–2556.

Weidmann, C., Spagnotto, S., Giménez, M., Martínez, P., Álvarez, O., Sánchez, M. & Lince Klinger, F. (2013). Crustal structure and tectonic setting of the south central Andes from gravimetric analysis. *Geofísica Internacional* **52**, 197–208.

Winpenny, B. & Maclennan, J. (2011). A partial record of mixing of mantle melts preserved in Icelandic phenocrysts. *Journal of Petrology* **52**, 1791–1812.